Multiwavelength View of the Close-by GRB 190829A Sheds Light on Gamma-Ray Burst Physics

Downloaded from: https://research.chalmers.se, 2026-10-15 05:34 UTC

Citation for the original published paper (version of record):
Salafia, O., Ravasio, M., Yang, J. et al (2022). Multiwavelength View of the Close-by GRB 190829A Sheds Light on Gamma-Ray Burst Physics. Astrophysical Journal Letters, 931(2).
http://dx.doi.org/10.3847/2041-8213/ac6c28

N.B. When citing this work, cite the original published paper.

research.chalmers.se offers the possibility of retrieving research publications produced at Chalmers University of Technology. It covers all kind of research output: articles, dissertations, conference papers, reports etc. since 2004. research.chalmers.se is administrated and maintained by Chalmers Library

(article starts on next page)

The Astrophysical Journal Letters, 931:L19 (21pp), 2022 June 1 https://doi.org/10.3847/2041-8213/ac6c28
© 2022. The Author(s). Published by the American Astronomical Society.
OPEN ACCESS

Multiwavelength View of the Close-by GRB 190829A Sheds Light on Gamma-Ray Burst Physics

Om Sharan Salafia[1,2,3], Maria Edvige Ravasio[1,3], Jun Yang[4], Tao An[5,6], Monica Orienti[7], Giancarlo Ghirlanda[1,2], Lara Nava[1,8], Marcello Giroletti[7], Prashanth Mohan[6], Riccardo Spinelli[1,9], Yingkang Zhang[5], Benito Marcote[10], Giuseppe Cimò[10], Xuefeng Wu[11], and Zhixuan Li[12]

[1] INAF–Osservatorio Astronomico di Brera, via E. Bianchi 46, I-23807 Merate (LC), Italy; omsharan.salafia@unmib.it
[2] INFN–Sezione di Milano-Bicocca, piazza della Scienza 3, I-20126 Milano (MI), Italy
[3] Università degli Studi di Milano-Bicocca, Dipartimento di Fisica "G. Occhialini", piazza della Scienza 3, I-20126 Milano (MI), Italy
[4] Department of Space, Earth and Environment, Chalmers University of Technology, Onsala Space Observatory, SE-439 92 Onsala, Sweden
[5] Shanghai Astronomical Observatory, Key Laboratory of Radio Astronomy, Chinese Academy of Sciences, Nandan Road 80, 200030, People's Republic of China
[6] Key Laboratory of Cognitive Radio and Information Processing, Guilin University of Electronic Technology, 541004, Guilin, People's Republic of China
[7] INAF–Istituto di Radioastronomia, via P. Gobetti 101, I-40129 Bologna, Italy
[8] INFN–Sezione di Trieste, via Valerio 2, I-34127 Trieste (TS), Italy
[9] Dipartimento di Scienza e Alta Tecnologia, Università dell'Insubria, Via Valleggio 11, I-22100 Como, Italy
[10] Joint Institute for VLBI ERIC, Oude Hoogeveensedijk 4, 7991 PD Dwingeloo, The Netherlands
[11] Purple Mountain Observatory, Chinese Academy of Sciences, Nanjing 210023, People's Republic of China
[12] Yunnan Observatories, Chinese Academy of Sciences, 650216 Kunming, Yunnan, People's Republic of China
Received 2022 February 18; revised 2022 April 26; accepted 2022 May 1; published 2022 May 27

Abstract

We monitored the position of the close-by (about 370 Mpc) gamma-ray burst GRB 190829A, which originated from a massive star collapse, through very long baseline interferometry (VLBI) observations with the European VLBI Network and the Very Long Baseline Array, carrying out a total of nine observations between 9 and 117 days after the gamma-ray burst at 5 and 15 GHz, with a typical resolution of a few milliarcseconds. From a state-of-the art analysis of these data, we obtained valuable limits on the source size and expansion rate. The limits are in agreement with the size evolution entailed by a detailed modeling of the multiwavelength light curves with a forward-plus-reverse shock model, which agrees with the observations across almost 18 orders of magnitude in frequency (including the HESS data at TeV photon energies) and more than 4 orders of magnitude in time. Thanks to the multiwavelength, high-cadence coverage of the afterglow, inherent degeneracies in the afterglow model are broken to a large extent, allowing us to capture some unique physical insights; we find a low prompt emission efficiency of $\lesssim 10^{-3}$, a low fraction of relativistic electrons in the forward shock downstream $\chi_e < 13\%$ (90% credible level), and a rapid decay of the magnetic field in the reverse shock downstream after the shock crossing. While our model assumes an on-axis jet, our VLBI astrometry is not sufficiently tight as to exclude any off-axis viewing angle, but we can exclude the line of sight to have been more than $\sim 2^\circ$ away from the border of the gamma-ray-producing region based on compactness arguments.

Unified Astronomy Thesaurus concepts: Gamma-ray bursts (629); Very long baseline interferometry (1769); Shocks (2086); Relativistic jets (1390); Relativistic aberration (1385)

1. Introduction

Radio observations of gamma-ray burst (GRB) afterglows have rarely been successful in constraining their projected size or proper motion due to the large distances involved. In a handful of cases (Taylor et al. 1998, 1999; Frail et al. 2000; Alexander et al. 2019), such as that of GRB 970508 (Frail et al. 1997), scintillation of the radio source induced by scattering of the emission by the interstellar medium has been used as an indirect probe of the source size. On the other hand, the only case so far in which very long baseline interferometry (VLBI) observations could produce a direct measurement of the size of a GRB afterglow is that of GRB 030329 (Taylor et al. 2004). More recently, VLBI observations of GRB 170817A (Mooley et al. 2018; Ghirlanda et al. 2019) led to direct inference of the effects of relativistic motion, that is, an apparently superluminal displacement of the source centroid. In these favorable cases, the joint modeling of the light curves and of the evolution of the apparent size (Mesler & Pihlström 2013) or the centroid displacement (Ghirlanda et al. 2019; Hotokezaka et al. 2019) helped to mitigate the problem of afterglow model degeneracies, which most often prevents the determination of the source's physical properties unless some parameters are fixed based on educated guesses.

At the other end of the electromagnetic spectrum, observations of GRB afterglows at teraelectronvolt (TeV) photon energies (Zhang & Mészáros 2001; Nava 2018) have also shown potential in breaking the modeling degeneracies and constrain the underlying physical processes. Such photon energies are, in principle, beyond the reach of synchrotron emission from shock-accelerated electrons (de Jager & Harding 1992; Nava 2018; Abdalla et al. 2021); inverse Compton scattering of the synchrotron photons by the same relativistic electrons (synchrotron self-Compton; Rybicki & Lightman 1979; Panaitescu & Mészáros 1998; Chiang & Dermer 1999; Panaitescu & Kumar 2000; Sari & Esin 2001) is expected to dominate at these energies. Such a process was shown to provide a viable explanation (Veres et al. 2019) for the TeV

Original content from this work may be used under the terms of the Creative Commons Attribution 4.0 licence. Any further distribution of this work must maintain attribution to the author(s) and the title of the work, journal citation and DOI.

Table 1
Summary of VLBI Observations and Image Parameters

UT (Duration)	Freq. (GHz)	VLBI Network[a]	Synth. Beam (Major × Minor, PA)	rms: σ_i (μJy beam^{-1})
Sep 17, 22:30 (8 hr)	4.99	EVN+e-MERLIN	3.38 × 2.16 mas^2, +35°.7	15.3
Oct 15, 21:00 (8 hr)	4.99	EVN+e-MERLIN	3.66 × 2.56 mas^2, +23°.2	10.4
Nov 12, 19:00 (8 hr)	4.99	EVN+e-MERLIN	4.16 × 2.79 mas^2, +19°.6	11.4
Sep 7, 07:56 (6 hr)	15.39	VLBA	1.76 × 0.60 mas^2, −10°.8	44.4
Oct 3, 06:14 (6 hr)	15.17	VLBA	1.86 × 0.68 mas^2, −9°.0	31.5
Sep 11, 07:30 (6 hr)	4.98	VLBA	2.16 × 2.16 mas^2, +0°.0	33.8
Oct 16, 05:30 (6 hr)	4.98	VLBA	3.32 × 1.31 mas^2, −1°.0	17.1
Nov 17, 03:15 (6 hr)	4.88	VLBA	5.44 × 2.02 mas^2, −4°.5	9.8
Dec 24, 00:45 (6 hr)	4.88	VLBA	3.33 × 1.26 mas^2, −2°.5	12.6

Note.
[a] The full list of VLBI stations is provided in the text.

emission component recently detected (MAGIC Collaboration 2019) by the Major Atmospheric Gamma-ray Imaging Cherenkov (MAGIC) telescopes in association with GRB 190114C. Different emission processes mean different dependencies on the physical properties of the source, which enhances the prospects for breaking the degeneracies. Unfortunately, TeV observations of GRBs are notoriously difficult, and only a few detections have been reported so far (Atkins et al. 2000; Abdalla et al. 2019; MAGIC Collaboration 2019; Blanch et al. 2020a, 2020b), including the source (de Naurois 2019; Abdalla et al. 2021) we study in this work.

2. Results

2.1. The GRB 190829A Event

The long GRB 190829A was detected by the Gamma-ray Burst Monitor (GBM) on board the Fermi satellite on 2019 August 29 at 19:55:53 UT (Fermi GBM Team 2019) and shortly thereafter (Dichiara et al. 2019) by the Burst Alert Telescope (BAT) on board the Neil Gehrels Swift Observatory (hereafter Swift). It is the third GRB detected (de Naurois 2019) at TeV photon energies after GRB 190114C (MAGIC Collaboration et al. 2019) and GRB 180720B (Abdalla et al. 2019), but compared to these, it features a smaller isotropic equivalent energy (Tsvetkova et al. 2019; $E_{\rm iso} \sim 3 \times 10^{50}$ erg; see also Appendix B). The redshift of the host galaxy, $z = 0.0785$ (Valeev et al. 2019; corresponding to a luminosity distance of approximately 368 Mpc adopting Planck cosmological parameters, Planck Collaboration 2016, or, equivalently, an angular diameter distance of 316 Mpc), makes this event one of the closest long GRBs known to date. The afterglow emission of GRB 190829A has been monitored up to several months after the burst; after an initial peak and a fading phase, a rebrightening in the optical light curve at ∼5 days was attributed to the associated supernova emission (confirmed by the spectroscopic observations of the 10.4 m Gran Telescopio Canarias telescope, GTC; Hu et al. 2021). Radio afterglow emission was first detected by the Australia Telescope Compact Array (ATCA) at 5.5 GHz (Laskar et al. 2019) and then by the Northern Extended Millimeter Array (NOEMA) at 90 GHz (de Ugarte Postigo et al. 2019), 20.2 and 29.48 hr after the burst, respectively. Subsequent high-cadence radio observations were performed with the Meer Karoo Array Telescope (MeerKAT) at 1.3 GHz and Arcminute Microkelvin Imager–Large Array (AMI-LA) at 15.5 GHz, reporting a fading radio source up to 143 days after the initial GRB (Rhodes et al. 2020).

2.2. VLBI Observations and Sedov Length Constraint

We conducted VLBI observations of GRB 190829A with the Very Long Baseline Array (VLBA) at 15 and 5 GHz and the European VLBI Network (EVN) alongside the enhanced Multi-Element Remotely Linked Interferometer Network (e-MERLIN) at 5 GHz, for a total of nine epochs between 9 and 116 days after the GRB (see Table 1).

Despite the good angular resolution reached in all observations, the source remained consistently unresolved. In order to obtain reliable upper limits on the source size, we fitted a circular Gaussian model to the data through a Markov Chain Monte Carlo (MCMC) approach (Appendix A.2), which we first tested against simulated sources immersed in real noise (Appendix A.3). From the analysis of our nine-epoch data, we obtained the limits reported in Table 2 and shown in Figure 1. Assuming an intrinsic source size evolution $s \propto t^{5/8}$, as expected (Granot et al. 1999) for the observed size s of a relativistic blast wave whose expansion is described by the self-similar Blandford–McKee solution (Blandford & McKee 1976), we could translate our measurements into a largely model-independent upper limit on the ratio between the blast-wave energy E and the number density n of the surrounding ambient medium, which sets the fundamental length scale of the expansion, namely, the Sedov length (Blandford & McKee 1976) $\ell_S = (3E/4\pi n m_p c^2)^{1/3}$, where m_p is the proton mass and c is the speed of light. Since (Blandford & McKee 1976; Granot et al. 1999) $s \propto \ell_S^{3/8} t^{5/8}$, we have that $E/n \propto \ell_S^3 \propto s^8 t^{-5}$. After carefully evaluating the proportionality constant (Appendix A.4) and adopting a flat prior on the source size, we obtained the posterior probabilities shown in Figure 2. We note that, since we do not resolve the source, only upper limits derived from these posteriors are meaningful. The most stringent upper limit is that from our first EVN epoch (solid blue line in Figure 2), which yielded $\log[(E/n)/\mathrm{erg\ cm^3}] < 55.6$ at the 90% credible level. After combining the posterior probabilities from all of the epochs (gray line in Figure 2; see Appendix A.4), we obtained $\log[(E/n)/\mathrm{erg\ cm^3}] < 54.1$ at the 90% credible level.

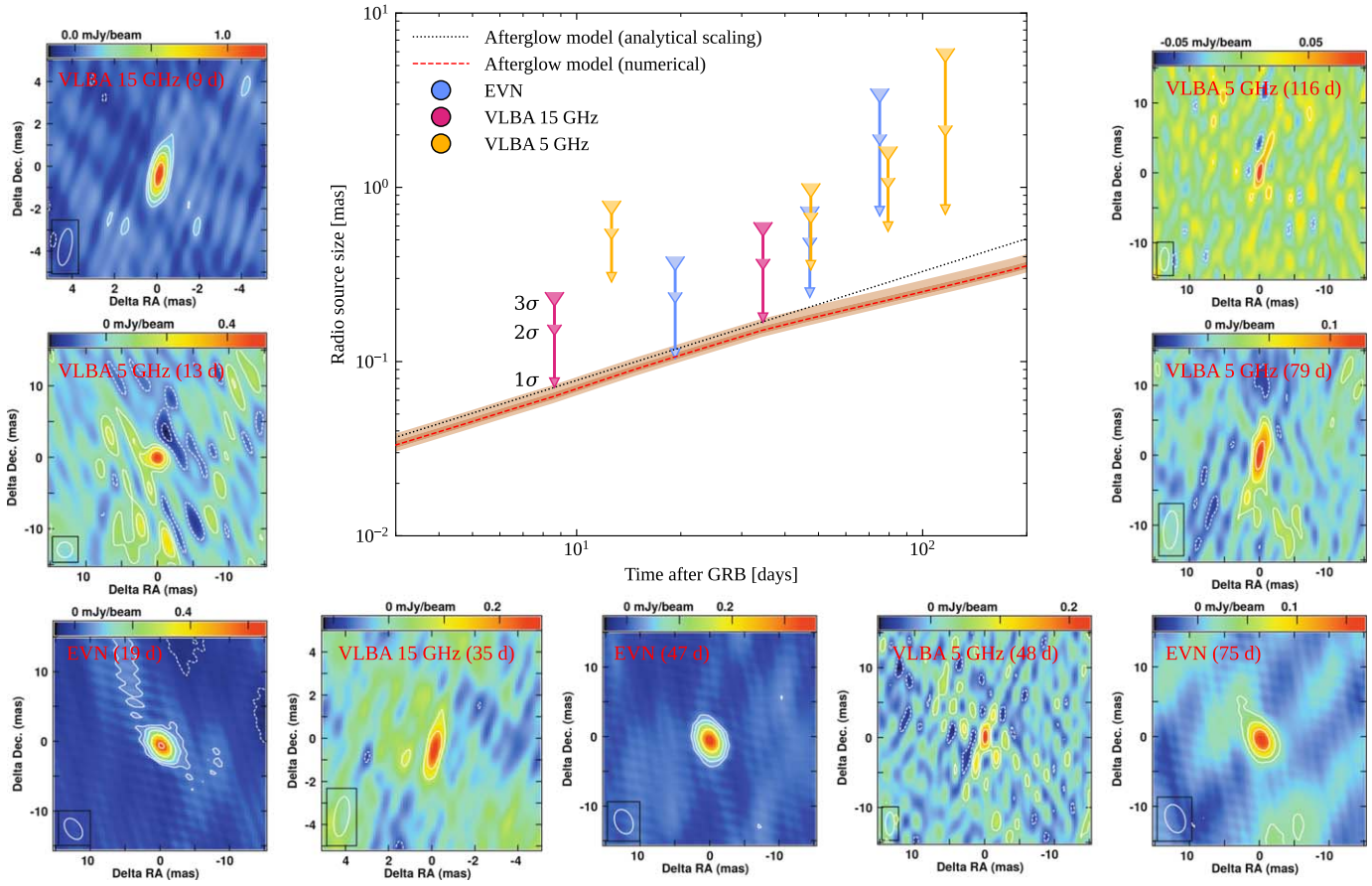

Figure 1. Source size upper limits and comparison with the model. In the middle panel, downward arrows show our 1σ, 2σ, and 3σ upper limits on the source size at each epoch (see Appendix A.4). The dashed lines show the source size evolution as predicted by our afterglow model (analytical $t^{5/8}$ scaling, Granot et al. 1999, in black; source size from our numerical model in red) assuming our best-fit parameters (see Appendix C.6). The pink shaded band shows the 90% credible interval implied by our afterglow parameter uncertainties. The surrounding smaller panels show previews of the cleaned radio maps for each epoch (full-size maps are available on Zenodo; see Salafia et al. 2022).

Table 2
Summary of the VLBI Imaging Results of GRB 190829A

Epoch	MJD (days)	Freq. (GHz)	$S_{\rm pk}$ (mJy beam^{-1})	$S_{\rm tot}$ (mJy)	$\theta_{\rm size,UL}$ (mas)	ΔR.A. (mas)	Δdecl. (mas)
1	2	3	4	5	6	7	8
EVN (19 days)	58,743.947	4.99	0.546 ± 0.017	$0.645^{+0.014}_{-0.016}$	0.189	$-0.032^{+0.028}_{-0.035}$	$-0.042^{+0.021}_{-0.028}$
EVN (47 days)	58,771.880	4.99	0.340 ± 0.011	$0.352^{+0.017}_{-0.011}$	0.381	$0.080^{+0.058}_{-0.047}$	$-0.004^{+0.045}_{-0.054}$
EVN (75 days)	58,799.797	4.99	0.164 ± 0.010	$0.168^{+0.016}_{-0.012}$	1.331	$-0.245^{+0.197}_{-0.090}$	$0.067^{+0.158}_{-0.120}$
VLBA (9 days)	58,733.338	15.39	1.080 ± 0.035	$1.245^{+0.064}_{-0.044}$	0.120	$0.117^{+0.015}_{-0.010}$	$-0.198^{+0.032}_{-0.032}$
VLBA (35 days)	58,759.267	15.17	0.241 ± 0.024	$0.275^{+0.033}_{-0.043}$	0.285	$0.102^{+0.053}_{-0.037}$	$-0.355^{+0.118}_{-0.118}$
VLBA (13 days)	58,737.323	4.98	0.523 ± 0.031	$0.581^{+0.019}_{-0.023}$	0.477	$3.106^{+0.018}_{-0.019}$	$3.378^{+0.034}_{-0.058}$
VLBA (48 days)	58,772.238	4.98	0.229 ± 0.017	$0.248^{+0.019}_{-0.014}$	0.549	$1.500^{+0.045}_{-0.044}$	$-0.314^{+0.084}_{-0.120}$
VLBA (79 days)	58,804.140	4.98	0.128 ± 0.010	$0.105^{+0.013}_{-0.012}$	0.889	$1.032^{+0.082}_{-0.109}$	$0.128^{+0.231}_{-0.220}$
VLBA (116 days)	58,841.039	4.98	0.092 ± 0.013	$0.060^{+0.030}_{-0.010}$	3.198	$1.254^{+0.198}_{-0.601}$	$-0.525^{+0.399}_{-0.480}$

Note. Columns give (1) epoch name as given in the main text, (2) Modified Julian Date (MJD), (3) observing frequency, and (4) peak brightness, followed by the the circular Gaussian model fitting results: (5) total flux density, (6) 90% credible upper limit on the angular size, i.e., FWHM, and (7) and (8) relative offsets (including the correction of the core shift at 15 GHz of 0.035 mas in R.A. and -0.408 mas in decl.; see text) in R.A. and decl. with respect to the reference position (J2000, R.A. $= 02^{\rm h}58^{\rm m}10\overset{\rm s}{.}52173$, decl. $= -08°57'28\overset{''}{.}0956$). The reported uncertainties are statistical 1σ errors; additional systematic uncertainties are discussed in the text.

2.3. Time-dependent Multiwavelength Modeling and Interpretation

In order to test this result and get a deeper physical insight on this source, we performed a self-consistent modeling of all of the available multiwavelength observations of the afterglow. We included both the forward and reverse shock emission in our model, assuming a uniform angular profile for all jet properties within an opening angle $\theta_{\rm j}$ and computing the shock

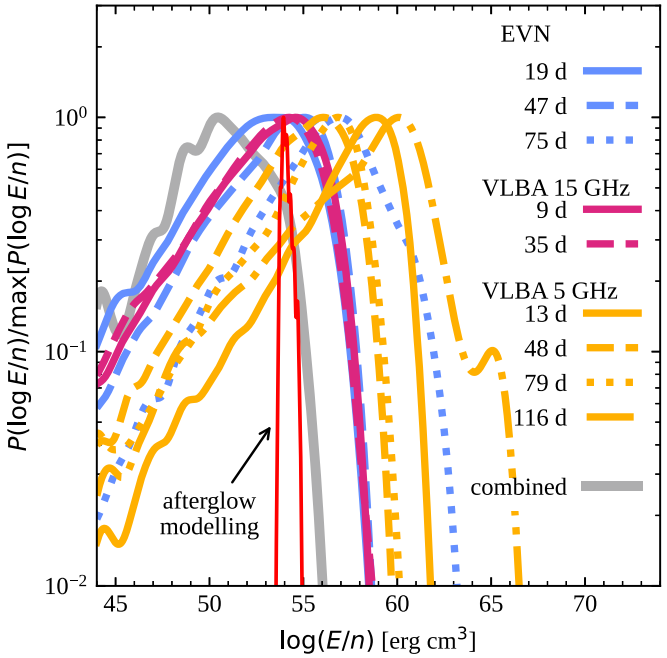

Figure 2. Constraint on the energy-to-density ratio. Blue, purple, and orange lines (same color coding as in Figure 1) show the posterior probability on $\log(E/n)$ obtained (Appendix A.4) from the source size measurements (Appendix A.2) in our VLBI imaging epochs assuming the source to be a relativistic shock in self-similar expansion (Blandford & McKee 1976; Granot et al. 1999). The gray line shows the combined posterior from all epochs. The thin red solid line is the posterior obtained from fitting our forward-plus-reverse shock afterglow emission model to the available multiwavelength data.

dynamics self-consistently from deceleration down to the late side expansion phase. We computed the radiation in the shock downstream comoving frame, including the effects of inverse Compton scattering on electron cooling (accounting for the Klein–Nishina suppression of the cross section above the relevant photon energy), assuming a fixed fraction ϵ_e of the available energy density to be in relativistic electrons (which we assumed to be a fraction χ_e of the total electrons and injected with a power-law energy distribution with index $p > 2$) and a fraction ϵ_B to be in the form of an effectively isotropic magnetic field. To compute the observed emission, we integrated over equal arrival time surfaces and considered relativistic beaming effects.

Figure 3 shows the GRB 190829A afterglow light curves in the X-ray, optical, and radio bands obtained by combining publicly available data (circles; see Appendix C.1) with the flux densities measured in our VLBI campaign (stars; see Appendix A.1). The lines represent the predictions of our best-fit afterglow model (Appendix C.4), where the dashed lines show the contribution from the reverse shock only, while the solid lines also include the forward shock, which dominates the emission at all wavelengths from around 1 day onward. In addition, Figure 4 shows the predicted spectral energy distributions (SEDs) at 5 (blue) and 30 (red) hr after the GRB, which agree with the emission detected (de Naurois 2019; Abdalla et al. 2021) by the High Energy Stereoscopic System (HESS; butterfly-shaped symbols show 1σ uncertainties, including systematics, when assuming a power-law spectral shape). In our interpretation, therefore, the HESS emission is synchrotron self-Compton from the forward shock. Different from what was reported in the main text of Abdalla et al. (2021), we do not find significant photon–photon absorption, at least for our model parameters (see Appendix C.5). From this modeling, we obtained $\log[(E/n)/\mathrm{erg\ cm^3}] = 53.9^{+0.4}_{-0.2}$ (90% credible level; posterior shown by the red line in Figure 2), in agreement with the VLBI size upper limits, as can also be appreciated from Figure 1, where the source size evolution entailed by the afterglow emission model (red dashed line) is compared with our source size upper limits. We regard our ability to interpret all of the available data self-consistently as a success of the standard GRB afterglow model, confirming our general understanding of these sources, but we stress that in order to obtain these results, we had to include a number of often overlooked (even though widely agreed upon in most cases) elements in the model.

The results of our afterglow model fitting (see Table 4 and Figure 11) provided some rather unique insights on the physics of GRBs and the forward and reverse shocks that form as the jet expands into the interstellar medium. Remarkably, we found that the usual simplifying assumption $\chi_e = 1$ in the forward shock is excluded (that is, we were unable to find a statistically acceptable solution when assuming all electrons in the shock downstream to be accelerated to relativistic speeds), and we had $\chi_e < 0.04$ at 90% credibility when adopting a wide prior $-10 < \log(\chi_e) < 0$. On the other hand, with such a wide prior, we found our uncertainty on the total (collimation-corrected, two-sided) jet kinetic energy to extend toward unrealistically large values $E_{\rm jet} = E/(1 - \cos\theta_{\rm jet}) \gtrsim 10^{53}$ erg (assuming two oppositely oriented, identical jets of half-opening angle $\theta_{\rm jet}$), corresponding to very small fractions of accelerated electrons $\chi_e \lesssim 10^{-3}$. When adopting a tighter prior, $-2 < \log(\chi_e) < 0$, motivated by particle-in-cell simulations of relativistic collisionless shocks (which typically find χ_e to be around a few percent; Spitkovsky 2008; Sironi & Spitkovsky 2011), we obtained best-fit values consistent within the uncertainties, but the unrealistic-energy tails were removed. In what follows, we report the results for this latter prior choice (we report 1σ credible intervals unless otherwise stated), while the results for the wider prior are given in Appendix C.6 (Table 4). The jet isotropic equivalent kinetic energy at the onset of the afterglow is $E = 2.5^{+1.9}_{-1.3} \times 10^{53}$ erg, and the jet half-opening angle is $\theta_{\rm jet} = 15.4^{+1.3\circ}_{-0.9}$, implying a total jet energy $E_{\rm jet} = 9^{+9}_{-4} \times 10^{51}$ erg, which is about half of the energy in the associated supernova (Hu et al. 2021). Given the observed gamma-ray isotropic equivalent energy $E_{\gamma,\rm iso} = (2.91 \pm 0.18) \times 10^{50}$ erg (see Appendix B), the implied gamma-ray efficiency is $\eta_\gamma = E_{\gamma,\rm iso}/(E_{\gamma,\rm iso} + E) = 1.2^{+1.0}_{-0.5} \times 10^{-3}$. This efficiency is much lower than the typical estimates for other GRBs in the literature (Fan & Piran 2006; Zhang et al. 2007; Wygoda et al. 2016; Beniamini et al. 2016), even though we note that a recently published study (Cunningham et al. 2020) of GRB 160625B also found a low efficiency when leaving the χ_e parameter free to vary. The prompt emission efficiency we find is compatible with that expected in the case of internal shocks within the jet (Rees & Meszaros 1994) with a moderate Lorentz factor contrast (Kumar 1999).

The jet bulk Lorentz factor before the onset of the deceleration is $\Gamma_0 = 57^{+4}_{-5}$. Considering the isotropic equivalent radiated energy $E_{\rm iso} \sim 3 \times 10^{50}$ erg, this is in agreement with the $\Gamma - E_{\rm iso}$ correlation found for long GRBs (Figure 12; see Ghirlanda et al. 2018).

The external medium number density (assumed constant) is relatively low, $n = 2.1^{+3.7}_{-1.0} \times 10^{-1}\,\mathrm{cm^{-3}}$. This could be tentatively explained by the large offset of the GRB location

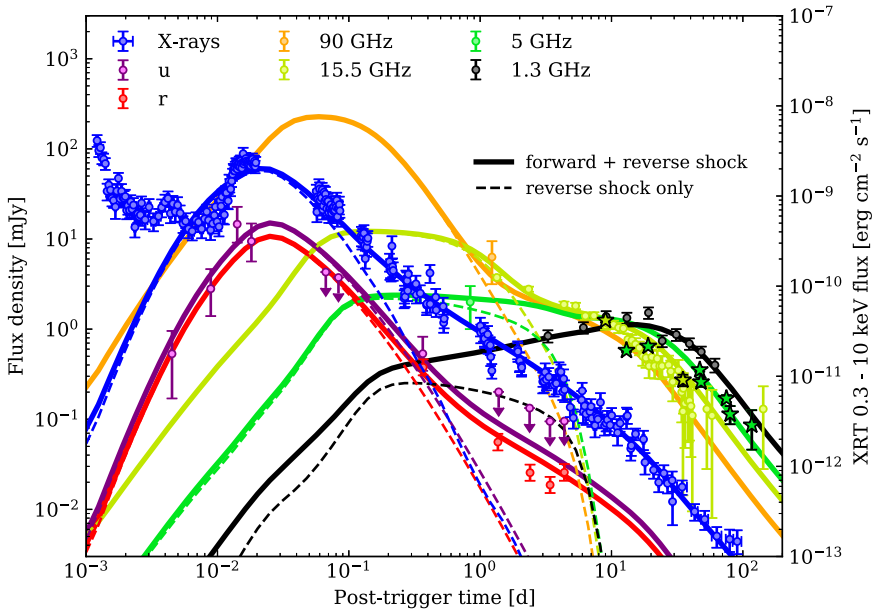

Figure 3. Multiwavelength data and emission model. Circles represent X-ray fluxes (blue; values shown on the right axis) or flux densities (all other colors; values shown on the left axis) measured at the position of GRB 190829A at different times after the GRB trigger in several bands (see the legend). Optical flux densities have been corrected for both the Milky Way and host galaxy extinction, and the contribution of the host galaxy has been subtracted. The host galaxy contribution (Rhodes et al. 2020) has also been subtracted from the AMI-LA radio flux densities at 15.5 GHz. Stars mark the flux densities measured in our VLBI epochs. Solid lines of the corresponding colors show the predictions of our emission model including both the forward and reverse shocks. Dashed lines single out the contribution of the reverse shock emission. We interpret the initial plateau in the X-ray data as the superposition of the prompt emission tail and the rising reverse shock emission.

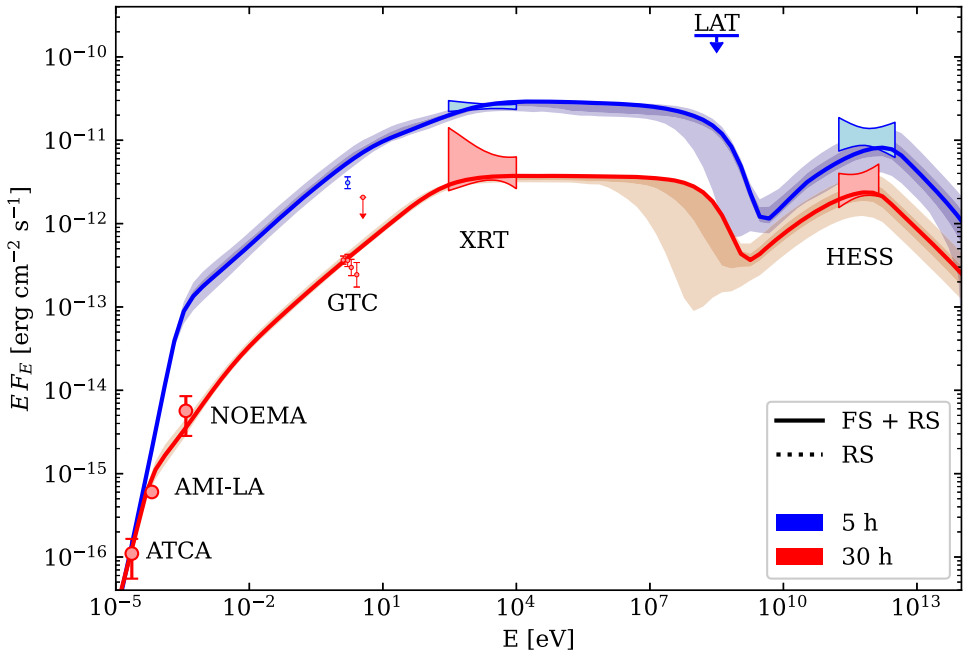

Figure 4. Predicted SEDs at the times of the HESS detections. We show with blue (red) solid lines our model at 5 hr (30 hr) after the gamma-ray trigger, with 90% and 50% credible bands in lighter shades. The HESS "butterflies" include the reported (Abdalla et al. 2021) systematic error contribution (summed in quadrature). We also show XRT butterflies at the corresponding times (from our own analysis; see Appendix C.3), plus GTC optical and NOEMA, ATCA, and AMI-LA radio data points taken at observing times lying within 0.2 dex.

with respect to the host galaxy center. Indeed, using the GRB coordinates derived from our VLBI observations and the host galaxy center position from the 2MASS catalog (Skrutskie et al. 2006), we measure a separation of $9\farcs6$, corresponding to a physical projected separation of 14.7 kpc. This is comparable to the largest previously measured offset in long GRBs (Blanchard et al. 2016; that of GRB 080928), placing it, in principle, in the underdense outskirts of its host galaxy. On the other hand, even though the surrounding interstellar medium density may be low, the associated supernova indicates that the progenitor must have been a massive star, which should have polluted the environment with its stellar wind. By contrast, the sharp increase in the flux density preceding the light-curve peak as seen in the optical and X-rays is inconsistent with a

wind-like external medium, which would result in a much shallower rise (Kobayashi & Zhang 2003). This places stringent constraints on the properties of the presupernova stellar wind, whose termination shock radius (van Marle et al. 2006) must be smaller than the nominal deceleration radius in the progenitor wind, $R_{\rm dec,w} = E/4\pi A m_{\rm p}\Gamma_0^2 c^2$. The parameter A sets the stellar wind density and can be expressed as a function of the wind mass-loss rate $\dot{M}_{\rm w}$ and velocity $v_{\rm w}$ as $A = 3\times10^{35}\dot{M}_{\rm w,-5}v_{\rm w,3} \equiv 3\times10^{35}A_\star$, where $\dot{M}_{\rm w,-5} = \dot{M}_{\rm w}/10^{-5}{\rm M}_\odot\,{\rm yr}^{-1}$ and $v_{\rm w,3} = v_{\rm w}/1000\,{\rm km\,s}^{-1}$. Requiring the wind termination shock radius (van Marle et al. 2006)—which depends on the wind properties, the external interstellar medium density n_0, and the progenitor lifetime $t_\star$—to be smaller than $R_{\rm dec,w}$, we obtain

$$\dot{M}_{\rm w,-5} < 3\times10^{-4}E_{52}^{10/13}\Gamma_{0,2}^{-20/13}v_{\rm w,3}^{9/13}n_{0,2}^{3/13}t_{\star,\rm Myr}^{-4/13}, \quad (1)$$

where $E_{52} = E/10^{52}$, $\Gamma_{0,2} = \Gamma_0/100$, $n_{0,2} = n_0/100\,{\rm cm}^{-3}$, and $t_{\star,\ \rm Myr} = t_\star/1$ Myr. Inserting our best-fit afterglow parameters, we obtain $\dot{M}_{\rm w,-5} < 7\times10^{-2}v_{\rm w,3}^{9/13}n_{0,2}^{3/13}t_{\star,\rm Myr}^{-4/13}$. For the fiducial wind speed, external interstellar medium density (here we set $n_0 = 100\,{\rm cm}^{-3}$ assuming that, despite the large offset, the progenitor was embedded in a star-forming region, but the dependence on this parameter is very weak), and progenitor lifetime parameters, this limits the wind mass-loss rate to $\dot{M}_{\rm w} < 7\times10^{-7}\,M_\odot\,{\rm yr}^{-1}$, which can be achieved only in the case of a very low metallicity or low Eddington ratio (Sander et al. 2020). Alternatively, the low wind mass-loss rate could be explained as the result of wind anisotropy induced by the fast rotation of the progenitor star (Ignace et al. 1996; Eldridge 2007), which would reduce the wind mass-loss rate along the stellar rotation axis.

For the forward shock, we found a relativistic electron power-law slope $p_{\rm FS} = 2.010^{+0.0021}_{-0.0025}$, reminiscent of that expected for first-order Fermi acceleration in nonrelativistic strong shocks (Bell 1978) and slightly lower than the $p\sim2.2$ expected for relativistic shocks (Sironi & Spitkovsky 2011). When p is close to (or below) 2, as in our case, the adopted value of the maximum electron energy $\gamma_{\rm max}$ starts impacting the normalization of the relativistic electron energy spectrum. For this reason, we also fitted an additional free parameter $\gamma_{\rm max}/\gamma_{\rm min}$, which sets the ratio (assumed constant throughout the evolution) of the maximum to the minimum electron energy in the injected relativistic electron power law. We find $\log(\gamma_{\rm max}/\gamma_{\rm min}) > 4.6$ at the 90% credible level. The 1σ credible interval on the fraction of accelerated electrons is $\chi_{\rm e,FS} = 2.3^{+1.1}_{-1.3}\times10^{-2}$ (note that the uncertainty extends down to $\chi_{\rm e}\sim10^{-3}$ when adopting the wider prior, see Table 4, as discussed above). The electron energy density fraction is $\epsilon_{\rm e,FS} = 3.0^{+2.9}_{-1.7}\times10^{-2}$, slightly lower than but comparable to the expected $\epsilon_{\rm e}\sim0.1$ for mildly relativistic, weakly magnetized shocks (Sironi & Spitkovsky 2011). On the contrary, the magnetic field energy density fraction is $\epsilon_{\rm B,FS} = 2.5^{+3.5}_{-1.3}\times10^{-5}$, in line with previous studies of GRB afterglows (Barniol Duran 2014; Wang et al. 2015), implying inefficient magnetic field amplification by turbulence behind the shock or a relatively fast decay of such turbulence with the distance from the shock front (Lemoine 2013, 2015). Interestingly, the best-fit values we found for the jet isotropic equivalent energy E, the interstellar medium number density n, and the forward shock microphysical parameters $\epsilon_{\rm e,FS}$ and $\epsilon_{\rm B,FS}$ all closely resemble those found (Veres et al. 2019) for another GRB recently detected at TeV energies, GRB 190114C, under the constant external density assumption.

For the reverse shock, we fixed $\chi_{\rm e,RS} = 1$ as usual to reduce the number of parameters, since we could not constrain it to be lower than this value. We found that, in order to be able to interpret the X-ray and optical peaks at $t\sim10^{-2}$ days as reverse shock emission (corresponding to the end of the reverse shock crossing; see Equation (C5)) without overpredicting (see the typical radio reverse shock light-curve shapes in Resmi & Zhang 2016, which show late-time bumps) the later radio data, the magnetic field in the shock downstream must have decayed rapidly after the reverse shock crossed the jet. In particular, we found that the magnetic energy density must have decayed at least as fast as $B^2\propto V^{-\eta_{\rm B}}$ with $\eta_{\rm B}\geqslant6$, where V is the comoving volume of the shell (see Appendix C.4 for a detailed description of the assumed dynamics before and after the shock crossing), different from the usual simplifying assumption (Kobayashi 2000) that $\epsilon_{\rm B}$ remains constant before and after the shock crossing. We consider this reasonable, since the magnetic field is expected (Chang et al. 2008) to decay due to Landau damping of the shock-generated turbulence (which produces the magnetic field) after the shock crossing. For $\eta_{\rm B}\geqslant6$, our results are independent of the exact value of $\eta_{\rm B}$, and we obtained $\epsilon_{\rm e,RS} = 0.28^{+0.32}_{-0.16}$ and $\epsilon_{\rm B,RS} = 1.2^{+1.8}_{-0.8}\times10^{-3}$ and the accelerated electron power-law index $p_{\rm RS} = 2.13^{+0.04}_{-0.08}$.

2.4. Viewing Angle Limits

The inference on the afterglow parameters described so far is based on the assumption of an on-axis viewing angle. On the other hand, a slightly off-axis viewing angle could explain the relatively low luminosity and low peak energy of the observed prompt emission (Sato et al. 2021). This would imply, however, some degree of proper motion in the VLBI images (Fernández et al. 2021), which can be tested, in principle, with our observations. Considering the EVN 5 GHz and VLBA 15 GHz epochs only, as these were performed under sufficiently homogeneous observing strategies and shared the same phase-reference calibrator (see Appendix A.1); the largest displacement compatible at 1σ with the absence of an observed proper motion in our data is 0.71 mas (1σ upper limit, including systematic errors, on the displacement between our first VLBA 15 GHz and our last EVN epoch, which are the two most widely separated in both time and centroid position). At the source distance, this corresponds to $\delta r_{\rm max} < 1.088$ pc from $t_0 = 7.89$ to $t_1 = 69.5$ rest-frame days separating the two observations. In order to turn this into a limit on the source properties, we note that the apparent displacement δr of an off-axis jet is bound to be smaller than, or at most equal to, the size increase δs of a spherical relativistic blast wave with the same E/n ratio (i.e., the same Sedov length) over the same time, since the jet can be thought of as a portion of that sphere. Again using the self-similar expansion law from Granot et al. (1999), a relativistic blast wave would need to have $\log[(E/n)/{\rm erg\,cm}^3] \geqslant 59.3$ in order to produce an expansion $\delta s \geqslant \delta r_{\rm max}$ over the same time range, which is well beyond any conceivable value for a GRB. This means that our astrometric measurements are not sufficiently precise to exclude any viewing angle.

A relatively tight limit on the viewing angle can be obtained, on the other hand, by requiring the jet to be optically thin to the photons we observed during the prompt emission. In particular, we performed the calculation of the optical depth to γ-ray

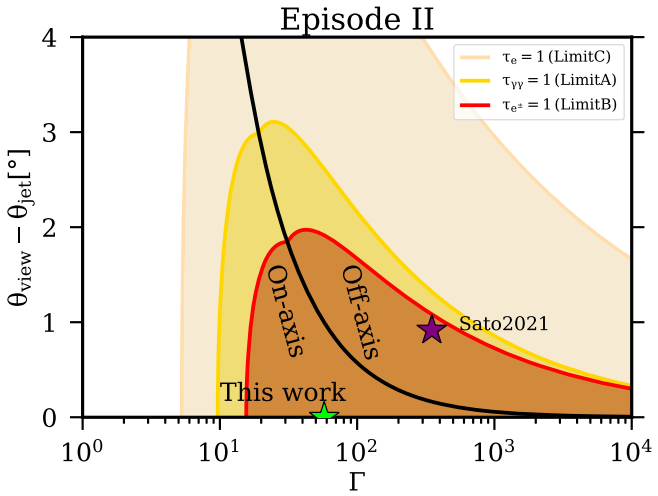

Figure 5. Limit on the viewing angle from compactness arguments on the prompt emission. Shaded areas show the allowed regions on the (Γ, $(\theta_{view} - \theta_{jet})$) plane, derived by the compactness limits A (photon–photon pair production), B (scattering off $e^{\pm}$), and C (scattering off e^{-} associated with baryons). The solid black line ($\Gamma\theta = 1$) separates on-axis observers from off-axis ones. The green star marks the bulk Lorentz factor Γ value inferred from the afterglow light-curve modeling, while the purple star marks the parameters used in Sato et al. (2021). Both solutions are in the allowed region that ensures that the source is transparent to the observed high-energy prompt emission photons.

photons for an arbitrary viewing angle and jet Lorentz factor (Matsumoto et al. 2019), given the observed spectrum. We focused on the brightest emission episode, namely, episode II, that provides the most stringent limit on the viewing angle. Photons of energy E must have been able to escape from the emitting region and not pair annihilate with other photons of energy $\geqslant(\delta m_e c^2)^2/E$, where δ is the relativistic Doppler factor $\delta = [\Gamma(1 - \beta\cos\theta)]^{-1}$ (limit A); must not have been scattered off by pairs produced by the annihilation of other high-energy photons (limit B); and must not have been scattered off by the electrons associated with the baryons in the outflow (limit C). The first two sources of opacity depend on the observed spectrum, while the third depends on the matter content of the jet, which we conservatively assumed to be the lowest compatible with the observed spectrum. Given the prompt emission spectrum observed in episode II, we computed the optical depth as a function of the bulk Lorentz factor Γ and viewing angle θ_{view} for limits A, B, and C following Matsumoto et al. (2019) and assumed an emission duration $\delta_t = 3$ s, which corresponds to the brightest peak in the emission episode. Figure 5 shows the regions on the Γ, $\theta_{view} - \theta_{jet}$ for which the optical depths are smaller than unity for the three limits. The solid black line corresponds to Γ $(\theta_{view} - \theta_{jet}) = 1$, therefore dividing the plot into on- and off-axis regions (inside or outside the relativistic beaming cone of material within the jet border). As shown in the plot, the value of Γ derived from our afterglow modeling (represented by the green star) is within the relatively small allowed region. The resulting upper limit on the viewing angle is $\theta_{view} - \theta_{jet} \lesssim 2°$ Adopting the jet opening angle $\theta_{jet} = 15°$ obtained from the afterglow modeling, a viewing angle greater than 17° would not be compatible with the observed emission.

Recently, a two-component jet model has been proposed (Sato et al. 2021) to explain the multiwavelength observations of GRB 190829A. In particular, a narrow ($\theta_{jet} = 0.015$, rad $= 0\overset{\circ}{.}86$) and fast ($\Gamma = 350$) jet was used to reproduce the bumps observed in the optical and X-rays at $t \sim 1.4 \times 10^3$ s from the trigger time, while a wide ($\theta_{jet} = 0.1$, rad $= 5\overset{\circ}{.}73$) and slow ($\Gamma = 20$) coaxial jet should explain the late ($t \gtrsim 10^5$ s) X-ray and radio emission. In this scenario, the observer is at an angle $\theta_{view} = 0.031$ rad ($1\overset{\circ}{.}78$) with respect to the jet axis. Since the authors of that work point out that the narrow jet could be responsible for the prompt emission of both episodes I and II, we also applied the compactness argument to this solution for comparison. As shown in Figure 5, the parameters they assumed for the narrow jet are still inside the allowed region, although quite close to its limit; therefore, the solution with an off-axis narrow jet as the source of the observed gamma rays is not ruled out from the compactness argument.

3. Summary and Discussion

Our VLBI observations and analysis results are compatible with the GRB 190829A afterglow being produced by a relativistic blast wave, at least at $t \geqslant 9$ days. We found that a forward-plus-reverse shock afterglow model, assuming an on-axis viewing angle and a uniform external medium density, is able to reproduce the observed light curves from the gamma rays down to the radio at 1.4 GHz, provided that only a relatively small fraction, $\chi_e \lesssim$ few $\times 10^{-2}$, of the electrons have been accelerated to relativistic speeds in the forward shock, and that the magnetic field in the reverse-shocked jet decays rapidly after the shock crossing. The required external medium density is homogeneous and relatively low, which points to a very weak progenitor stellar wind. The size evolution entailed by the model is in agreement with the limits set by our VLBI observations. On the other hand, while our calculations are based on the assumption of an on-axis jet, our analysis cannot exclude a viewing angle slightly off the jet border, in which case our derived parameters (especially those related to the reverse shock) would possibly require some modification. The jet and forward shock parameters obtained from our analysis are similar to those found (Veres et al. 2019) for GRB 190114C in the constant external density scenario.

As a final note, we point out that other interpretations of this GRB, differing from the one presented in this paper, have been proposed in the literature. The main point of qualitative disagreement among these interpretations is the X-ray/optical peak at $t \sim 10^{-2}$ days (i.e., around 10^3 s). Zhang et al. (2020) attributed it to late central engine activity; Lu-Lu et al. (2021) invoked the interaction of the blast wave with a preaccelerated electron–positron pair enriched shell formed due to annihilation of prompt emission photons, partly scattered by the dusty external medium; and Fraija et al. (2021) proposed a magnetar spin-down-powered origin. Given that the reverse shock is a natural consequence of the jet interaction with the external medium, our interpretation (within which we are able to explain all of the data self-consistently) can be preferred with respect to these based on Occam's razor. Finally, Rhodes et al. (2020) proposed a forward-plus-reverse shock interpretation. In contrast with us, though, they attributed the 15.5 GHz data at $t > 1$ day to a reverse shock in the thick shell regime. We note that, in this regime, the reverse shock emission would peak at the end of the prompt emission (around 70 s post-trigger), so that the X-ray/optical peak would remain unexplained.

O.S. thanks Marco Landoni and the Information and Communication Technologies (ICT) office of the Italian

National Institute for Astrophysics (INAF) for giving access to the computational resources needed to complete this work; he also acknowledges the Italian Ministry of University and Research (MUR) grant "FIGARO" (1.05.06.13), the INAF Prin 2017 (1.05.01.88.06), and the MUR Prin 2017 (20179ZF5KS) for financial support. T.A., P.M., and Y.K.Z. made use of the computing resources of the China SKA Regional Centre prototype under support from the National Key R&D Programme of China (grant No. 2018YFA0404603), NSFC (12041301), and Youth Innovation Promotion Association of CAS. G.G. acknowledges support from MIUR and PRIN 2017 (grant 20179ZF5KS). B.M. acknowledges support from the Spanish Ministerio de Economía y Competitividad (MINECO) under grant AYA2016-76012-C3-1-P and the Spanish Ministerio de Ciencia e Innovación under grants PID2019-105510GB-C31 and CEX2019-000918-M of ICCUB (Unidad de Excelencia "María de Maeztu" 2020–2023). The European VLBI Network (EVN) is a joint facility of independent European, African, Asian, and North American radio astronomy institutes. Scientific results from data presented in this publication are derived from the following EVN project code (s): EG010. The e-VLBI research infrastructure in Europe is supported by the European Union's Seventh Framework Programme (FP7/2007-2013) under grant agreement No. RI-261525 NEXPReS. e-MERLIN is a National Facility operated by the University of Manchester at Jodrell Bank Observatory on behalf of STFC. The research leading to these results has received funding from the European Commission Horizon 2020 Research and Innovation Programme under grant agreement No. 730562 (RadioNet). The National Radio Astronomy Observatory is a facility of the National Science Foundation operated under cooperative agreement by Associated Universities, Inc. Scientific results from data presented in this publication are derived from the following VLBA project codes: BA140, BO062. This work made use of the Swinburne University of Technology software correlator, developed as part of the Australian Major National Research Facilities Programme and operated under license. This work made use of data supplied by the UK Swift Science Data Centre at the University of Leicester.

The European Very Long Baseline Interferometry Network data (PIs: Ghirlanda & An) whose analysis has been presented in this study are publicly available at the EVN Data Archive at JIVE[13] under the identifiers RG010A, RG010B, and RG010C. The Very Long Baseline Array data are publicly available at the National Radio Astronomy Observatory (NRAO) Data Archive[14] under the identifiers BO062 (5 GHz epochs; PI: Orienti) and BA140 (15 GHz epochs; PI: An). The Neil Gehrels Swift Observatory data analyzed in this study are publicly available at the UK Swift Data Centre[15] at the University of Leicester. The Fermi/GBM data analyzed in this study are publicly available at the National Aeronautics and Space Administration (NASA) High-Energy Astrophysics Science Archive Research Centre (HEASARC) Fermi GBM Burst Catalog.[16] All reduced data and computer code are available from the corresponding authors upon reasonable request.

[13] http://www.jive.nl/select-experiment
[14] https://science.nrao.edu/facilities/vlba/data-archive
[15] https://www.swift.ac.uk/xrt_spectra
[16] https://heasarc.gsfc.nasa.gov/W3Browse/fermi/fermigbrst.html

Appendix A
VLBI Observations and Data Analysis

A.1. VLBA and EVN Observations and Data Reduction

We performed rapid-response VLBI observations of GRB 190829A with the VLBA and EVN plus the enhanced e-MERLIN. All of the observations were carried out in phase-referencing (Beasley & Conway 1995) mode.

The EVN plus e-MERLIN observations at 5 GHz were performed under project code RG010 (PI: Ghirlanda & An) in three epochs (2019 September 17, October 15, and November 12) with a total of 20 participating telescopes, namely, the Jodrell Bank MK II (Jb), Westerbork single antenna (Wb), Effelsberg (Ef), Medicina (Mc), Onsala (On), Tianma (T6), Toruń (Tr), Yebes (Ys), Hartebeesthoek (Hh), Svetloe (Sv), Zelenchukskaya (Zc), Badary (Bd), Irebene 16 m (Ib), Irebene 32 m (Ir), Cambridge (Cm), Darnhall (Da), Pickmere (Pi), Defford (De), Knockin (Kn), and Kunming (Km). Stations that missed the observations were T6, Ys, and Kn in the first epoch, Tr and Km in the second epoch, and Sv and Km in the last epoch. The EVN observations were carried out in electronic-VLBI mode (Szomoru 2008), and the data correlation was done in real time by the EVN software correlator (Keimpema et al. 2015) at the Joint Institute for VLBI ERIC using an integration time of 1 s and a frequency resolution of 0.5 MHz. The results are summarized in Table 1.

In the first epoch, we observed two phase calibrators, J0257–1212 and J0300–0846. Object J0257–1212 had a correlation amplitude (Charlot et al. 2020) of $\gtrsim$0.2 Jy at 8.4 GHz and an angular separation of 3°.24 away from the target source on the plane of the sky. Object J0300–0846 had a correlation amplitude of $\sim$0.02 Jy at 5 GHz on the long baselines (Petrov 2020) and a separation of 0°.56. The cycle times for the nodding observations of J0257–1212 and GRB 190829A were about 3 minutes at the lower observing elevation in the first and last 2 hr and about 6 minutes at the higher elevation in the middle 4 hr. The secondary calibrator J0300–0846 was observed for a short 2 minute scan every three cycles. In our observing strategy, the nearby weak calibrator J0300–0846 was the phase-referencing calibrator, and the bright calibrator J0257–1212 was mainly used to significantly boost the phase coherence time to about 1 hr in the post–data reduction.

Because the closer calibrator J0300–0846 also had a high correlation amplitude on the long baselines in the first-epoch observation, we optimized the observing strategy in the remaining two epochs; J0300–0846 was observed more frequently as a traditional phase-referencing calibrator, and J0257–1212 was observed as a fringe finder for only a few short scans. The cycle times were increased to about 4 minutes at lower elevations and about 7 minutes at higher elevations.

The data were calibrated with the National Radio Astronomy Observatory (NRAO) software package Astronomical Image Processing System (AIPS; Greisen 2003). We first flagged out some off-source or very low sensitivity visibility data. In the first epoch, the e-MERLIN stations Cm and De had unusually high fringe rates ($\gtrsim$10 mHz) owing to variable delays of their optical cables. Those data were excluded to avoid poor phase connections and some low-level baseline-based errors. The a priori amplitude calibration was done with properly smoothed antenna monitoring data (system temperatures and gain curves) or nominal system equivalent flux densities. The ionospheric

dispersive delays were corrected by using the maps of total electron content provided by the global positioning system satellite observations. The time-dependent phase offsets due to the antenna parallactic angle variations were removed. We aligned the phases across the subbands via iterative fringe fitting with a short scan of the calibrator data. After phase alignment, we combined all of the subband data in the Stokes *RR* and *LL*, then ran the fringe fitting with a sensitive station as the reference station and applied the solutions to all of the related sources. In the first epoch, after transferring the fringe-fitting solutions from J0257–1212 to both J0300–0846 and GRB 190829A, we also ran fringe fitting on J0300–0846 to solve for only phases and group delays and then transferred the solutions to GRB 190829A. In this additional iteration, we found that the Tr data had poor phase connections in the last 4 hr and the Ib data had large residual delays (∼1 ns), probably due to the uncertainty of their antenna positions or poor weather conditions during the observation. Because of these issues, we excluded these problematic data. Finally, bandpass calibration was performed. All of the above calibration steps were scripted in the ParselTongue (Kettenis et al. 2006) interface.

We imaged the calibrators J0257–1212 and J0300–0846 through iterative model fitting with a group of delta functions (point-source models) and self-calibration in Difmap (Shepherd et al. 1994). With the input source images, the fringe fitting and self-calibration were reperformed in AIPS via a ParselTongue script. All of these phase and amplitude solutions were also transferred to the target source data by linear interpolation. The final imaging results of the calibrator J0300–0846 are shown in supplementary figures available in the associated Zenodo repository (Salafia et al. 2022). They show a one-sided core–jet structure toward the north. The total flux densities are ∼34 mJy on September 17, ∼41 mJy on October 15, and ∼37 mJy on November 12. The compact radio core was modeled by a single point source. In the phase-referencing astrometry, we used the radio peak as the reference point, $03^{h}00^{m}19\overset{s}{.}5876$, $-08°46'10\overset{''}{.}174$ (J2000). Compared to the latest VLBI global solutions in the radio fundamental catalog (Petrov 2020) 2020b, the correction is quite small (ΔR.A.$= +0\overset{s}{.}000012 \pm 0.00003$, Δdecl.$= +0\overset{''}{.}00053 \pm 0\overset{''}{.}00110$) and thus dropped out in the differential astrometry. The bright calibrator J0257–1212 had flux densities of ∼320 mJy on September 17, ∼360 mJy on October 15, and ∼320 mJy on November 12.

We imaged GRB 190829A in Difmap without self-calibration. To avoid bandwidth smearing effects, we shifted the target to a position close (<1 mas) to the image center with the AIPS task UVFIX. To improve the phase coherence, we excluded the data observed at low elevations, i.e., $\leqslant 15°$.

We also carried out VLBA observations of GRB 190829A (project code: BA140; PI: An) at 15 GHz in two epochs (2019 September 7 and October 3; 6 hr each). All 10 VLBA antennas were used during the observations, namely, St. Croix (Sc), Hancock (Hn), North Liberty (Nl), Fort Davis (Fd), Los Alamos (La), Pie Town (Pt), Kitt Peak (Kp), Owens Valley (Ov), Brewster (Br), and Mauna Kea (Mk). The data were correlated by a distributed FX-style software correlator (DiFX; Deller et al. 2007) at the National Radio Astronomy Observatory. The output data had an integration time of 1 s and a frequency resolution of 0.5 MHz. Table 1 summarizes the results of these observations.

The VLBA 15 GHz observations of GRB 190829A had the same observing strategy as the first-epoch EVN plus e-MERLIN observations. Both J0257–1212 and J0300–0846 were observed. At 15 GHz, we used two cycle times: ∼110 s (scan lengths: 20 s for J0257–1212, 70 s for GRB 190829A or J0300–0846) in the first and last hour and ∼140 s (scan lengths: 20 s for J0257–1212, 100 s for GRB 190829A or J0300–0846) in the middle 4 hr. Object J0300–0846 was treated as a pseudotarget during the observations. Every six or seven cycles, there was a cycle for J0300–0846. The bright (>1 Jy at 15 GHz) radio sources 0234+285 and NRAO 150 were observed as the fringe finders. While similar to the EVN strategy, the procedure worked overall better because of the shorter cycle times and the higher mean elevation of the decl. $\sim -9°$ target for the VLBA stations.

Post–data reduction was carried out with AIPS and Difmap installed in the China SKA Regional Centre prototype (An et al. 2019). The calibration strategy in AIPS was basically the same as that used in the EVN plus e-MERLIN observations described above. The correlator digital correction was applied when the data were loaded into AIPS. Deviations in cross-correlation amplitudes owing to errors in sampler thresholds were corrected using the autocorrelation data. The atmospheric opacity was solved and removed using the system temperature data measured at each station. The a priori amplitude calibration was made with properly smoothed system temperatures and gain curves. The correction on the Earth orientation parameters was applied. Ionospheric dispersive delays were corrected according to maps of total electron content. Phase offsets due to antenna parallactic angle variations were removed. After the fringe fitting on the fringe finders, bandpass calibration was performed. We ran a global fringe fitting on J0257–1212 and applied the solutions to both J0300–0846 and GRB 190829A. After that, we ran another global fringe fitting on the weak calibrator J0300–0846 by switching off the solutions of the residual fringe rate and used a low signal-to-noise ratio (S/N) cutoff of 3. With such setups, we got more accurate phase and delay solutions, in particular for the long-baseline data.

We then imaged the calibrators J0257–1212 and J0300–0846 in Difmap. The self-calibration and imaging procedure at 15 GHz was the same as that at 5 GHz. Object J0257–1212 shows a one-sided core–jet structure with total flux densities of 0.36 ± 0.02 Jy in the first epoch and 0.38 ± 0.02 Jy in the second one. The correlation amplitude is quite high, $\gtrsim$0.15 Jy on all baselines.

The imaging results of J0300–0846 are displayed in supplementary figures available in the associated Zenodo repository (Salafia et al. 2022). Object J0300–0846 has a core–jet structure with total flux densities of ∼22 mJy in the first epoch and ∼26 mJy in the second epoch. In both epochs, the visibility data of J0300–0846 could be simply fitted with four point-source models. After the two calibrator images were made, we reran the fringe fitting to remove source structure-dependent phase errors. To improve the amplitude calibration further, we also applied the self-calibration amplitude solutions of J0257–1212 to the data of GRB 190829A in AIPS.

As a starting point, we used the radio core of J0300–0846 as the reference position at 15 GHz, as we did for 5 GHz. We noticed, though, that the partially self-absorbed radio core of J0300–0846 has a frequency-dependent positional shift (the so-called "core shift" effect; Kovalev et al. 2008) mainly along the

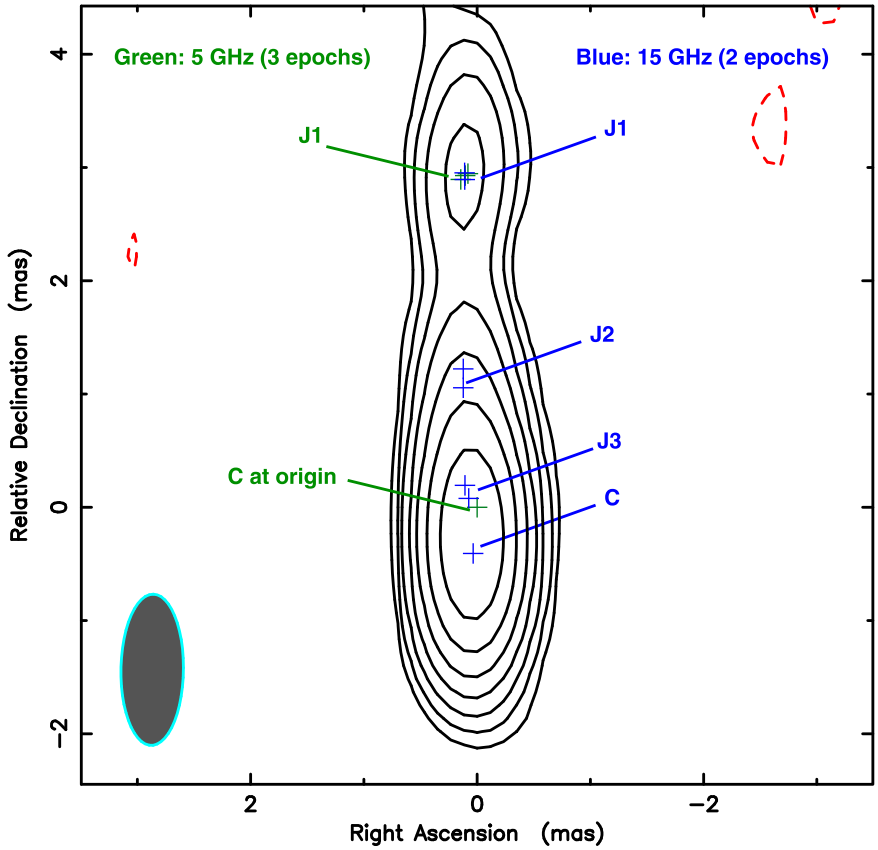

Figure 6. Frequency-dependent shift of the initial reference point C from 5 to 15 GHz. The best-fit point-source models are plotted as green plus signs at 5 GHz and blue plus signs at 15 GHz. The contours show the 15 GHz image at the second epoch. Using the mean position of the optically thin, discrete, and compact jet component J1 as the reference point, the shift was derived and corrected in the joint astrometry.

jet direction (see Figure 6). Using the mean position of the compact (size $\leqslant$0.22 mas), relatively discrete, and steep-spectrum component J1 as the reference point, we corrected the frequency-dependent shift of the initial reference point C from 5 to 15 GHz. The 15 GHz component C has a mean positional shift of ΔR.A. $= 0.035 \pm 0.008$ mas, Δdecl. $= -0.408 \pm 0.019$ mas with respect to the 5 GHz component C. The jet component J1 had flux densities of 5.3 ± 0.3 mJy at 5 GHz and 1.6 ± 0.1 mJy at 15 GHz, implying an optically thin spectrum ($dF/d\nu \propto \nu^{-1.04\pm0.07}$), and its position therefore has a negligible frequency dependence. Because of the high redshift (Hewett & Wild 2010) $z = 1.862$ and the short time baseline, the positional shift of J1 between any two epochs is quite small, $\leqslant$0.063 mas in R.A. or decl.

We imaged GRB 190829A at 15 GHz adopting the same procedure as for the EVN data. To avoid bandwidth smearing effects, we also shifted its position before doing any average. To improve the phase-referencing precision, we excluded the data observed at the low elevations of $\leqslant 50^\circ$ for the near-sea station SC and $\leqslant 30^\circ$ for the rest of the stations.

An additional set of VLBA observations of GRB 190829A triggered by the TeV detection (de Naurois 2019) were carried out at 5 GHz (C band; project code BO062; PI: Orienti) for a total of four epochs between 2019 September and December (see Table 1 for details). Observations were performed with a recording bandwidth of 128 MHz and a 2048 Mbps data rate, with the exception of the last two epochs, which made use of a 4 Gbps data rate. We centered the observation of the first epoch at (Paek et al. 2019) R.A. (J2000) $= 02^{\rm h}58^{\rm m}10\overset{\rm s}{.}510$, decl. (J2000) $= -08^\circ57'28\overset{''}{.}44$, whereas the observations of the following epochs were centered at R.A. (J2000) $= 02^{\rm h}58^{\rm m}10\overset{\rm s}{.}5219$, decl. (J2000) $= -08^\circ57'28\overset{''}{.}0933$ based on the results of the first observation.

During each observing run, the target source was observed for about 4 hr in phase-referencing mode. Scans on the target were bracketed by scans on the phase calibrator J0257−1212. In addition, every hour, we spent a 3 minute scan on the phase-referencing check source J0253−1200 at about $1\overset{\circ}{.}07$ from the phase-reference source. Considering the time on the target source, calibrations, and overhead, the total observing time for each run was about 6 hr.

Editing and a priori calibration were performed following standard procedures as described above and also in the AIPS cookbook, correcting for ionospheric dispersive delays, digital sampling corrections, parallactic angle variations, and instrumental delays. We calibrated the bandpass using a scan on 3C 84 in which all of the antennas had good data. Amplitudes were calibrated using the antenna system temperatures and antenna gains. Uncertainties on the amplitude scale, $\sigma_{\rm cal}$, were about 7%. We performed global fringe fitting to correct for residual fringe delays and rates. Since the target source is too faint for fringe fitting, we applied the solutions of the phase-reference calibrator J0257−1212 to the target and the check source J0253−1200. We also fringe-fitted the check source in order to compare the flux density obtained with and without fringe fitting. The two values were in good agreement.

Images were produced using the task IMAGR in AIPS. The source is clearly detected in all epochs. We performed the analysis for determining the astrometry, but the angular

separation to the phase-referencing calibrator was proven to be too large, preventing an accurate determination of the position (uncertainties of about 0.3 mas); therefore, these data were of no use in constraining any potential source projected motion.

The final imaging results of GRB 190829A are shown in supplementary figures available in the associated Zenodo repository (Salafia et al. 2022). The synthesized beams and the image noise levels are reported in Table 1. The target GRB 190829A was clearly detected in all nine epochs with S/Ns ranging from 10 to 31. Moreover, the VLBI observations at the same observing frequency had quite similar coverages of the (u, v)-plane.

The peak flux densities and the circular Gaussian model fitting results are tabulated in Table 2.

Besides the fitting uncertainties reported in Table 2, we included in the error budget systematic positional uncertainties of 0.051 mas in R.A. and 0.075 mas in decl. for the EVN and VLBA 15 GHz epochs and 0.3 mas in R.A. and 0.4 mas in decl. for the VLBA 5 GHz epochs. These stem from a statistical study (Paragi et al. 2013) of four-epoch VLBA phase-referencing observations of a pair of extragalactic sources (J1707−1415 and NVSS3; separation: $1^{\circ}.89$) at 5 GHz whose reported 1σ scatters are 0.17 mas in R.A. and 0.25 mas in decl. Our systematic uncertainty estimates were derived by rescaling these values by the ratio (0.3 for EVN and VLBA 15 GHz; 1.7 for VLBA 5 GHz) of our target source–phase reference source angular separation to that of the cited study, due to the fact that systematic positional uncertainties are generally proportional to angular separations in VLBI phase-referencing astrometry (Kirsten et al. 2015). Because GRB 190829A has a relatively low decl. and there are more east–west long-baseline data, as shown in supplementary figures available in the associated Zenodo repository (Salafia et al. 2022), the astrometry precision in R.A. is always better than that in decl. Compared to the EVN astrometry at 5 GHz, the VLBA astrometry at 15 GHz might have somewhat smaller systematic errors because of the higher observing elevation at most VLBA stations and the more uniform antenna sensitivities.

As a side note, we have searched for compact radio components in the central region (2.46×2.46 arcsec^2) of the host galaxy (Heintz et al. 2019; Rhodes et al. 2020) SDSS J025810.28−085719.2 with the wide-field imaging function provided by the AIPS task IMAGR. We find no compact radio emission with a brightness $\geqslant 0.056$ mJy beam^{-1} (6σ) at 5 GHz. To search for any extended radio emission, we also tried to use a taper of 0.3 at a (u, v) radius of five megawavelengths. With a large beam size of 30×22 mas^2, still no emission above 5σ ($\geqslant 0.14$ mJy beam^{-1}) was seen in the dirty maps.

A.2. VLBI Data Source Model Fitting

In order to obtain detailed information about the source total flux density, size, and position from each of our VLBI epochs, we fitted the calibrated visibility data adopting an MCMC approach. We adopted a simple Gaussian likelihood model, namely,

$$\ln \mathcal{L}(x) = -\frac{1}{2}\sum_{i=0}^{N} w_i[(\mathcal{V}_{R,\mathrm{m}}(u_i, v_i, x) - \mathcal{V}_{R,i})^2 + (\mathcal{V}_{I,\mathrm{m}}(u_i, v_i, x) - \mathcal{V}_{I,i})^2], \quad \text{(A1)}$$

where $\mathcal{V}_{R,i}$ and $\mathcal{V}_{I,i}$ are the real and imaginary parts, respectively, of the ith visibility measurement, corresponding to position (u_i, v_i) on the (u,v) plane, and w_i is its AIPS-determined data weight (corresponding to the reciprocal of the square of the associated uncertainty). Here $\mathcal{V}_{R,\mathrm{m}}(u, v, x)$ and $\mathcal{V}_{I,\mathrm{m}}(u, v, x)$ are the real and imaginary parts of the model source visibility, which we took as a circular Gaussian, evaluated at point (u,v) with parameters $x = (f_\nu, s, \rho, \delta)$, f_ν being the total flux density at the observing frequency, s the FWHM, and ρ and δ the spherical offsets of the source with respect to the phase center. With these definitions, one has

$$\mathcal{V}_{\mathrm{m}} = f_\nu e^{-2\pi^2\left(\frac{s}{\sqrt{8\ln 2}}\right)^2 (u^2+v^2) - 2\pi i(u\rho + v\delta)}, \quad \text{(A2)}$$

where $i = \sqrt{-1}$. We sampled the posterior probability of the parameters using the EMCEE (Foreman-Mackey et al. 2013) python package and adopting a uniform prior on all parameters with the constraints $f_\nu > 0$ and $10^{-6} < s/\mathrm{mas} < 10$. We initialized EMCEE with the best-fit parameters obtained by fitting the source to a circular Gaussian in DIFMAP and ran 10^4 iterations of the MCMC with eight walkers, for a total of 8×10^4 evaluations of the posterior probability density, of which we discard the initial half as burn-in. Corner plots constructed using the resulting posterior samples are available on Zenodo (Salafia et al. 2022). We took the parameter values corresponding to the sample with the highest posterior probability density as our best fit, and we estimated the 1σ credible range of each parameter as the smallest interval containing 68% of the marginalized posterior probability and the 95% credible size upper limits as the 95th percentile of the posterior samples. All results are reported in Table 2, and the size upper limits are shown in Figure 1.

A.3. VLBI Source Parameter Estimation: Validation on Simulated Sources

In order to validate our Bayesian parameter estimation approach, we ran our MCMC fitting procedure on several simulated data sets to check whether (and how well) the injected source parameters were recovered. The simulated observations were created by adding a fake circular Gaussian source to the calibrated visibilities of our October 3 VLBA 15 GHz observations (the choice of this particular observation was based on its low S/N, which ensured a minimal interference of the actual GRB source on our results). We performed the experiment several times, varying the S/N between 15 and 120 and the size of the fake source between 0.1 and 3 times the synthesized beam size.

According to Martí-Vidal et al. (2012), the possibility of overresolving a source (i.e., being able to resolve it despite its size being smaller than the synthesized beam) depends critically on the parameter $\omega = \mathrm{S/N(size/beam)}^2$ (see their Equation (7)), with $\omega \sim 1$ being the threshold below which the source cannot be resolved (the exact threshold depends on the array characteristics). Figure 7 reports the results of our simulations, showing how the marginalized posterior probability density of the source size depends on the ω over-resolution parameter. Our results are in excellent agreement with those of Martí-Vidal et al. (2012), and they show that our chosen priors are well behaved and that the analysis leads to unbiased results.

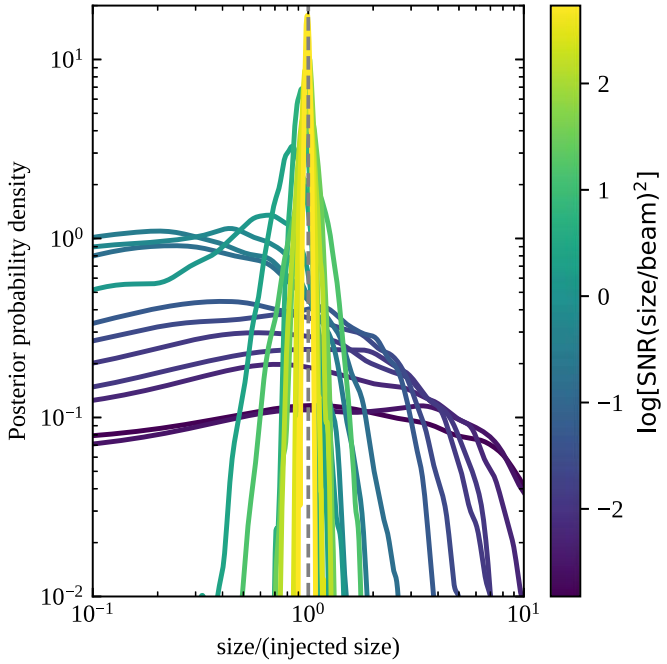

Figure 7. Marginalized source size posterior probability density for simulated sources immersed in real noise. Solid curves, color-coded by the overresolution parameter (Martí-Vidal et al. 2012) $\omega = \mathrm{S/N(size/beam)}^2$, show the marginalized posterior probability density of the source size (in units of the injected size) obtained by applying our MCMC-based fitting procedure to simulated circular Gaussian sources immersed in the noise of our October 3 VLBA 15 GHz observation. For $\omega \gtrsim 1$, the source starts to be clearly distinguishable from a point source.

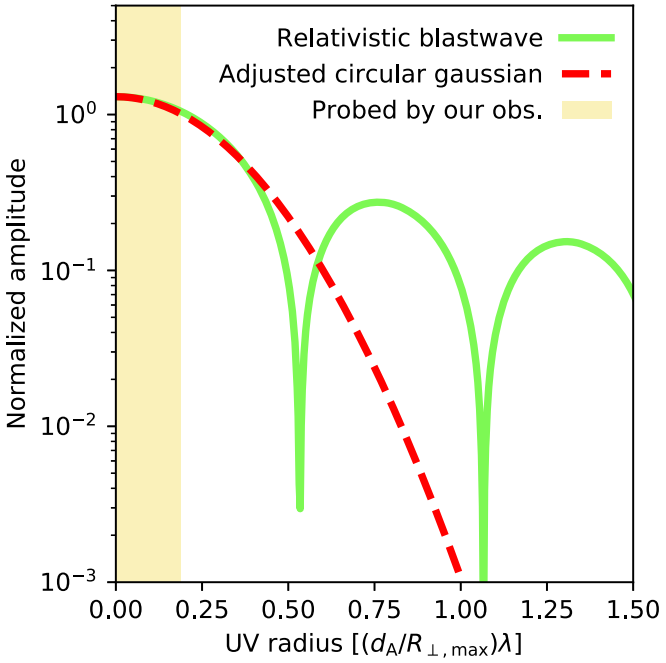

Figure 8. Comparison of the visibility amplitude dependence on the *UV* radius for a circular Gaussian and a relativistic blast wave (Granot et al. 1999). The circular Gaussian size has been adjusted to match the first peak of the blast wave; see text.

A.4. Relativistic Blast-wave Source Size and Sedov Length Constraint

Our VLBI size measurements are obtained assuming a circular Gaussian source visibility model. In order to compare these to the expected size of a relativistic blast wave, we investigated the visibility amplitude dependence on the *UV* radius for the brightness profile from Granot et al. (1999), which is a limb-brightened disk whose physical radius is given by $R_{\perp,\mathrm{max}} = 3.9 \times 10^{16}(E_{52}/n)^{1/8}(t_{\mathrm{obs}}/(1+z)\mathrm{days})^{5/8}\,\mathrm{cm}$. We find the shape of the first peak in the visibility amplitudes to be essentially independent of the similarity variable (Granot et al. 1999) ϕ as long as $0.1 < \phi < 10$, which comfortably accommodates our observations.

In Figure 8, we plot the amplitude as a function of the *UV* radius for $\phi = 1$ (green solid line), along with that corresponding to a circular Gaussian (red dashed line) with a size (FWHM) $s = 0.65 \times 2 \times R_{\perp,\mathrm{max}}/d_A$, where d_A is the angular diameter distance. This demonstrates that, as long as the longest baselines are shorter than $\sim 0.4 d_A/R_{\perp,\mathrm{max}}$ wavelengths, such a circular Gaussian accurately reproduces the expected amplitudes. Our longest baselines extended to $\sim 160\,M\lambda$, which is well below this limit at the times of our observations. This allowed us to make the identification $s = 0.65 \times 2 \times R_{\perp,\mathrm{max}}/d_A$, where s is the FWHM of our circular Gaussian model. Inverting this, we obtained $\log(E/n) = 52 + 8\log(s) - 5\log(t_{\mathrm{obs}}/(1+z)\mathrm{days}) - 8\log(5.08 \times 10^{16}\ \mathrm{cm}/d_A)$. This relation allowed us to turn the likelihood $\mathcal{L}(d_i \mid s, t_{\mathrm{obs},i})$ of the ith observation (here d_i represents the corresponding visibility data set, $t_{\mathrm{obs},i}$ represents the time at which the observation was performed, and the likelihood is marginalized over all variables but the source size) into a $\log(E/n)$ likelihood. By Bayes' theorem, the posterior probability density is $P(\log(E/n) \mid d_i) \propto \mathcal{L}(d_i \mid \log(E/n), t_{\mathrm{obs},i})\pi(\log(E/n))$, where the last term is the prior on $\log(E/n)$. Our flat prior on the source size s corresponds to a prior $\pi(\log(E/n)) \propto (E/n)^{1/8}$. We note that in our afterglow modeling, given the chosen priors (see Table 4), the effective prior on $x = \log(E/n) = \log(E) - \log(n)$ is instead

$$\pi(x) \propto \begin{cases} x - x_{\mathrm{min}} & x_{\mathrm{min}} \leqslant x < (x_{\mathrm{min}} + x_{\mathrm{max}})/2 \\ x_{\mathrm{max}} - x & (x_{\mathrm{min}} + x_{\mathrm{max}})/2 \leqslant x \leqslant x_{\mathrm{max}} \end{cases}, \quad \text{(A3)}$$

where $x_{\mathrm{max}} = \log(E_{\mathrm{max}}/n_{\mathrm{min}})$ and $x_{\mathrm{min}} = \log(E_{\mathrm{min}}/n_{\mathrm{max}})$. Here E_{min}, E_{max}, n_{min}, and n_{max} represent the prior bounds on E and n as reported in Table 4. For the comparison in Figure 2, therefore, we divided the afterglow posterior by this prior and multiplied it by $(E/n)^{1/8}$ in order to keep the prior consistent in the comparison (the effect is anyway negligible, as the likelihood is strongly peaked).

Since the size measurements are independent, their likelihoods could be combined by multiplication, so that the posterior probability of $\log(E/n)$ from the entire data set could be expressed as $P(\log(E/n) \mid \boldsymbol{d}) \propto \pi(\log(E/n))\Pi_{i=1}^{9}\mathcal{L}(d_i \mid \log(E/n), t_{\mathrm{obs},i})$. The resulting posterior probability densities are shown in Figure 2. From the combined epochs, we obtained $E/n < 10^{54.1}\,\mathrm{erg\,cm^3}$ at the 90% credible level (we only report the upper limit, since the lower bound is entirely determined by our prior). The (much tighter but more model-dependent) estimate of E/n we obtained from the multiwavelength modeling of the afterglow emission (red line in Figure 2) is in agreement with this upper limit.

Appendix B
Prompt Emission: Fermi/GBM Data Reduction

The prompt emission light curve of GRB 190829A shows the presence of two emission episodes (we refer to these as episodes I and II) separated by ∼50 s. We analyzed the spectra of the two prompt emission episodes detected by Fermi/GBM (Meegan et al. 2009). The spectral data files and corresponding latest response matrix files (rsp2) were obtained from the online HEASARC archive.[17] Spectra were extracted using the public software GTBURST. We analyzed the data of the three most illuminated NaI detectors with a viewing angle smaller than 60° (n6, n7, and n9) and the most illuminated BGO detector (b1). In particular, we selected the energy channels in the range 8–900 keV for the NaI detectors, excluding the channels in the range 30–40 keV (because of the iodine K edge at 33.17 keV), and 0.3–40 MeV for the BGO detector. We used intercalibration factors among the detectors, scaled to the most illuminated NaI and free to vary within 30%. To model the background, we manually selected time intervals before and after the burst and modeled them with a polynomial function whose order is automatically found by GTBURST. The spectral analysis was performed with the public software XSPEC (v. 12.10.1f). We used the PG-Statistic, valid for Poisson data with a Gaussian background, in the fitting procedure.

For episode I, we performed a time-integrated analysis from −1.79 to 10.5 s after the GBM trigger and fitted the spectra with two models, namely, a power law with an exponential cutoff and the Band function (namely, two power laws smoothly connected at the peak through an exponential transition). We compared the models based on the Akaike information criterion (AIC; Akaike 1974), finding that both fit the spectra equally well ($\Delta\mathrm{AIC} \leqslant 3$), but the β parameter in the Band function fit has large uncertainties. We therefore considered the cutoff power law as the best-fitting model of episode I, with the best-fitting parameters $\alpha = -1.63^{+0.09}_{-0.08}$, $E_c = 380^{+318}_{-134}$ keV, and $F = 1.98^{+0.07}_{-0.58} \times 10^{-7}$ erg cm^{-2} s^{-1}, where α is the low-energy spectral index, E_c is the scale energy of the spectral cutoff, and F is the flux integrated in the energy range 10 keV—10 MeV. With these parameters, the peak of the νF_ν spectrum is at $E_p = 139.7^{+57.1}_{-21.3}$ keV, and the isotropic equivalent energy is $E_{iso} = 1.02^{+0.10}_{-0.12} \times 10^{49}$ erg.

For episode II, we performed a time-integrated analysis in the interval 47.04–62.46 s with the same approach. The best-fitting model in this case is the Band function with $\alpha = -0.602^{+0.002}_{-0.358}$, $E_p = 11.30^{+0.39}_{-0.90}$ keV, $\beta = -2.52^{+0.01}_{-0.02}$, and $F = 7.56^{+0.12}_{-0.11} \times 10^{-7}$ erg cm^{-2} s^{-1}, where E_p is the peak photon energy of the νF_ν spectrum and α and β are the low- and high-energy spectral indices, respectively. For the second episode, the isotropic equivalent energy is $E_{iso} = 2.81^{+0.17}_{-0.15} \times 10^{50}$ erg. The results of the spectral analysis of the prompt emission are consistent with those previously published in the literature, e.g., Lesage et al. (2019), Hu et al. (2021), Fraija et al. (2021), and Chand et al. (2020).

[17] https://heasarc.gsfc.nasa.gov/W3Browse/fermi/fermigbrst.html

Appendix C
Afterglow: Data Reduction and Modeling

C.1. Data Collection from the Literature

We constructed an extensive GRB 190829A afterglow data set combining publicly available data, the results of our VLBI flux density measurements, and our own analysis of Swift/UVOT data. We obtained the Swift/XRT unabsorbed flux light curve shown in Figure 3 from the Burst Analyzer provided by the United Kingdom Swift Science Data Centre (Evans et al. 2010). The r-band optical data are from GTC observations from which the host galaxy contribution has been subtracted, as described in Hu et al. (2021). At times $0.1 < t/\mathrm{days} < 1$, a possible excess due to the underlying supernova could be present. The u-band data are the result of our own analysis of publicly available Swift/UVOT data, described below. The radio data comprise ATCA and NOEMA measurements described in the main text, AMI-LA and MeerKAT data from Rhodes et al. (2020), and our own flux densities as reported in Table 2 and shown with stars in Figure 3. An estimated host galaxy contribution (Rhodes et al. 2020) of $f_{\mathrm{host,15.5\ GHz}} = 0.15 \pm 0.1$ mJy has been subtracted from the AMI-LA data and the uncertainty summed in quadrature. Data points that result in upper limits after this subtraction are not shown in Figure 3 for presentation purposes but are included in the afterglow model fitting. Optical and ultraviolet data have been corrected for the Milky Way interstellar dust extinction (Schlafly et al. 2016) assuming $E(B-V) = 0.05$ and the host galaxy extinction adopting a Small Magellanic Cloud extinction curve and $E(B-V) = 1 \pm 0.1$, following Chand et al. (2020). The resulting systematic uncertainty in the flux density has been summed in quadrature to the flux density measurement errors.

C.2. UVOT Data Reduction

The UVOT images taken with the u filter were analyzed with the public HEASOFT (VERSION 6.25) software package. The most recent version of the calibration database was used. An ultraviolet candidate counterpart is detected 246 s after the BAT trigger at a position consistent with GRB 190829A. Photometry was performed within a circular source-extraction region of 3″ in radius. The background was extracted from a circular region with a radius of about 20″, close to our target but without contamination from other sources. We created the light curve (Figure 3) of the UVOT data using the `uvotproduct` tool, combining subsequent exposures until a significance of at least 3σ was reached. To estimate the contamination from the host galaxy, we stacked all of the u-band observations together with the tool `uvotimsum`. We performed photometry on this stacked image within three selected circular regions (of 3″ in radius) only containing host galaxy emission at a similar separation from the galactic nucleus (∼9″) as GRB 190829A and along the galactic plane. The ultraviolet contribution of the host galaxy at the position of GRB 190829A was estimated as the mean flux density of these three regions, with a conservatively estimated uncertainty equal to the statistical and systematic errors plus the standard deviation

Table 3
Best-fit Parameters of the XRT Data Spectral Analysis for the Two SED Epochs Coincident with HESS Observations, as Reported in Figure 4

Time Interval (hr)	Flux @ 1 keV (10^{-2} ph s^{-1} cm^2 keV)	Photon Index	C-Stat/DOF
[4.89–7.85]	$1.60^{+0.11}_{-0.07}$	$2.01^{+0.04}_{-0.05}$	398/420
[29.02–29.16]	$0.38^{+0.11}_{-0.09}$	$2.10^{+0.23}_{-0.28}$	43.5/280

of the three regions summed in quadrature. The resulting contaminant host galaxy flux density was then subtracted from the flux densities obtained through `uvotproduct`. Low-significance points at times >1 day were considered as upper limits, given the tighter limits from GTC (Hu et al. 2021).

C.3. Swift/XRT Data Reduction

In order to build the SEDs at the times of the HESS observations and check our model predictions, shown in Figure 4, we retrieved the XRT spectral files from the Swift/XRT online archive.[18] We analyzed the spectral files with the public software XSPEC (v. 12.10.1f). We excluded the energy channels below 0.3 keV and above 10 keV. Each spectrum is modeled with an absorbed power law using the Tuebingen–Boulder interstellar dust absorption model (Wilms et al. 2000) available in XSPEC. In particular, we used the `tbabs` model for the Galactic absorption (using $N_{\rm H} = 0.056 \times 10^{22}$ cm^{-2}; Kalberla et al. 2005) and the `ztbabs` model for the host galaxy absorption, adopting the source redshift $z = 0.0785$. The intrinsic $N_{\rm H}$ was fixed to the value obtained from the time-resolved analysis of late XRT data. Indeed, in the 0.3–10 keV energy range, the fitted values of $N_{\rm H}$ and the spectral index are closely correlated; a larger value of $N_{\rm H}$ allows for a softer spectrum, and vice versa, so that the net result of their combination is consistent with the observed spectrum. As a consequence, the intrinsic variations in the spectral index can be misinterpreted as variations of $N_{\rm H}$ when both of these parameters are free to vary. Since no $N_{\rm H}$ variation is expected at the times we analyzed, we performed a time-resolved spectral analysis of the XRT data up to 10^7 s after the Fermi/BAT trigger by leaving both the host $N_{\rm H}$ and the photon index free. We found that, at late times (from 2.8×10^4 s onward), the $N_{\rm H}$ parameter does not evolve and remains constant around $N_{\rm H} = 1.16 \times 10^{22}$ cm^{-2}. We therefore fitted the XRT spectra shown in Figure 4 assuming the abovementioned value of the intrinsic $N_{\rm H}$ and leaving as free parameters the normalization and spectral index of the power law. The results of the spectral analysis of the XRT data are reported in Table 3. We note that the results of the spectral analysis are consistent with those previously published in the literature for similar integration times (Abdalla et al. 2021).

C.4. Afterglow Model

C.4.1. Dynamics during the Reverse Shock Crossing

During the reverse shock crossing, we described the system as consisting of four regions separated by the forward shock, contact discontinuity, and reverse shock, respectively. We assumed all hydrodynamic quantities in each region to be uniform; that is, we neglected the shock profiles. Region 1 is the unperturbed external medium, which we assumed to be cold and have a uniform number density n. Region 2 is the shocked ambient medium, region 3 is the shocked jet material, and region 4 is the unperturbed jet material. We assumed regions 2 and 3 to move with the same Lorentz factor Γ during this phase, and we assumed the adiabatic index in both regions to be $\hat{\gamma} = 4/3$; that is, we assumed their pressure to be always radiation-dominated. Pressure balance across the contact discontinuity requires the internal energy densities in the two regions to be equal, namely, $e'_{\rm int,2} = e'_{\rm int,3}$. Relativistic Rankine–Hugoniot jump conditions at the forward shock set $e'_{\rm int,2} = e'_{\rm int,3} = (\hat{\gamma}\Gamma + 1)(\Gamma - 1)nm_{\rm p}c^2/(\hat{\gamma} - 1)$, where $m_{\rm p}$ is the proton mass, and $n'_{\rm e,2} = (\hat{\gamma}\Gamma + 1)n/(\hat{\gamma} - 1)$. The number density in region 4 is given by $n'_{\rm e,4} = E_0/(4\pi R^2 \Delta'_4 \Gamma_0 m_{\rm p} c^2)$, where E_0 is the total isotropic equivalent jet kinetic energy, and $\Delta'_4(R) = \max[\Gamma_0 cT, R/\Gamma_0]$, where T is the jet duration in the central engine frame, and we are assuming that the radial spreading of the jet becomes effective beyond the spreading radius $R_{\rm s} = \Gamma_0^2 cT$, after which the jet thickness in the central engine frame is (Kobayashi & Sari 2000) R/Γ_0^2. Since the reverse shock is well separated in time from the prompt emission, the shell was in the spreading phase at the time of deceleration, and the dynamics is therefore independent (Kobayashi 2000) of T (the so-called "thin shell" regime). Shock jump conditions set $n'_{\rm e,3} = (\hat{\gamma}\Gamma_{3,4} + 1)n/(\hat{\gamma} - 1)$, where $\Gamma_{3,4} = \Gamma_0\Gamma(1 - \beta_0\beta)$, and $\beta_0 = \sqrt{1 - \Gamma_0^{-2}}$. The forward shock Lorentz factor, as measured in the central engine frame, is (Blandford & McKee 1976) $\Gamma_{\rm s,2} = ((\Gamma + 1)/(\hat{\gamma}(2 - \hat{\gamma})(\Gamma - 1) + 2))^{1/2}(\hat{\gamma}(\Gamma - 1) + 1)$. The same relation holds for the reverse shock Lorentz factor as measured in frame 3, changing Γ with $\Gamma_{3,4}$. The reverse shock Lorentz factor $\Gamma_{\rm s,3}$ in the central engine frame was then obtained by the proper Lorentz transform. The amount of jet energy that crosses the reverse shock per unit radius advance is (Nava et al. 2013)

$$\frac{dE}{dR} = \frac{\beta_0 - \beta_{\rm s,3}}{\beta_{\rm s,2}} \frac{E_0 \Gamma_0}{\Delta'_4}, \tag{C1}$$

where $\beta_{\rm s,2} = \sqrt{1 - \Gamma_{\rm s,2}^{-2}}$ and $\beta_{\rm s,3} = \sqrt{1 - \Gamma_{\rm s,3}^{-2}}$, which can be integrated to give the jet energy that crossed the reverse shock at a given radius, $E(R)$. The comoving volume of regions 2 and 3 is $V'_i = 4\pi R^2 \Delta'_i$, with $i = 2, 3$. The thickness is set by electron (or baryon) number conservation, which yields $\Delta'_3 = (\hat{\gamma} - 1)\Delta'_4 E(R)/(\hat{\gamma}\Gamma_{3,4} + 1)\Gamma_0 E_0$ and $\Delta'_2 = (\hat{\gamma} - 1)R/3(\hat{\gamma}\Gamma_{3,4} + 1)$. The internal energy in region 2 is therefore $E_{\rm int,2} = e'_{\rm int,2} V'_2$; similarly, that in region 3 is $E_{\rm int,3} = e'_{\rm int,3} V'_3$. Finally, the mass swept by the forward shock is $m(R) = 4\pi R^3 nm_{\rm p}/3$. All of these relations allowed us to write the energy conservation equation

$$E(R) + m(R)c^2 = \Gamma(R)E(R)/\Gamma_0 + \Gamma_{\rm eff}(R)[E_{\rm int,2}(R) + E_{\rm int,3}(R)], \tag{C2}$$

where $\Gamma_{\rm eff} = (\hat{\gamma}\Gamma^2 - \hat{\gamma} + 1)/\Gamma$ provides the proper transformation of the internal energies in the central engine rest frame (Nava et al. 2013). To compute the dynamical evolution, we started by assuming that the jet did not decelerate appreciably at a small initial radius $R_0 = 10^{10}$ cm, where we set $E(R_0) = 0$, $\Gamma(R_0) = \Gamma_0$, $E_{\rm int,3} = 0$, and $E_{\rm int,2} = (\Gamma_0 - 1)m(R_0)c^2$. We then iteratively advanced the radius by small logarithmic steps,

[18] https://www.swift.ac.uk/xrt_spectra

numerically solving Equation (C2) for Γ at each radius and integrating Equation (C1) by the Euler method.

To account for the effect of side expansion, we assumed regions separated by angular distances $\theta_{s,0} = \Gamma_0^{-1}$ to be initially causally connected by pressure waves, and we assumed that the effective angle of causal connection θ_s increases as

$$\frac{d\theta_s}{dR} = \frac{\beta_{\rm sound}}{\beta\Gamma}, \tag{C3}$$

where $\beta_{\rm sound} = \sqrt{\hat{\gamma}(\hat{\gamma}-1)(\Gamma-1)/(1+\hat{\gamma}(\Gamma-1))}$ is the proper sound speed behind the forward shock (Kirk & Duffy 1999). We integrated Equation (C3) by the Euler method to obtain $\theta_s(R)$. This computation proceeded from this phase into the subsequent phase after the reverse shock crossing was complete. We assumed the effective opening angle of the jet to be $\theta_j(R) = \max[\theta_j(R_0), \theta_s(R)]$; that is, we assumed the jet to expand sideways at the local sound speed (Huang et al. 1999; Lamb et al. 2018) as soon as the angular size of the causally connected regions exceeded the initial angular size of the jet. The effect of side expansion on the dynamics is essentially that of diluting the jet energy over a larger solid angle, which we modeled simply by the substitution $E \to E(1-\cos\theta_j(R_0))/(1-\cos\theta_j(R))$ in Equation (C2). We also accounted for this in computing the comoving number and energy densities that we used for the synchrotron emission modeling.

C.4.2. Dynamics after Reverse Shock Crossing

The condition $E = E_0$ marks the radius at which the reverse shock completely crosses the jet. In the thin shell regime (the relevant regime in our case), this happens approximately at the "decleration" radius,

$$R_{\rm dec} = \ell_S \Gamma_0^{-2/3}, \tag{C4}$$

where $\ell_S = (3E_0/4\pi\, n\, m_p c^2)^{1/3}$ is the Sedov length. In the observer frame, this radius is crossed approximately at a time

$$t_{\rm dec} = \frac{R_{\rm dec}}{2\Gamma_0^2 c} \sim 10^{-2} E_{0,53}^{1/3} n_{-1}^{-1/3} \Gamma_{0,2}^{-8/3}\ {\rm days}, \tag{C5}$$

which corresponds to the peak time of the reverse shock emission.

From that radius on, we considered the evolution of the forward-shocked external medium material (region 2) as separated from that of the reverse-shocked jet material (region 3). In the thin shell regime (the relevant regime in our case; Kobayashi 2000), region 3 is expected to decelerate and expand adiabatically (Kobayashi 2000), transferring its energy (Kobayashi & Sari 2000) to region 2, which continues its expansion in a self-similar manner (Blandford & McKee 1976). We assumed (Kobayashi 2000) region 3 to decelerate as $\Gamma_3 \propto R^{-g}$, and we adopted the usual value (Kobayashi 2000), $g = 2$, which is consistent with the results of relativistic hydrodynamical simulations (Kobayashi & Sari 2000). Adopting a polytropic equation of state $e'_3 \propto n'^{\hat{\gamma}}_{e,3}$, the local sound speed is $c_{s,3} \propto n'^{(\hat{\gamma}-1)/2}_{e,3}$, which implies a comoving volume expansion $V'_3 \propto R^{(2g+6)/(\hat{\gamma}+1)}$. The internal energy therefore goes as $E'_{\rm int,3} \propto V'^{-1/3}_3 \propto R^{-(2g+6)/(3\hat{\gamma}+3)}$, and the number density simply decreases as $n'_{e,3} \propto V'^{-1}_3$. The initial conditions are given by the forward–reverse shock dynamics as computed in the previous section, and we kept the adiabatic index $\hat{\gamma} = 4/3$ fixed throughout this phase. This completely describes the evolution of region 2 after the shock crossing. For the evolution of region 2, we used a simplified energy conservation law (Panaitescu & Kumar 2000),

$$E_{\rm dyn} + mc^2 = \Gamma E_{\rm dyn}/\Gamma_0 + \Gamma^2 mc^2, \tag{C6}$$

which can be solved analytically (therefore speeding up the computation) and gives rather accurate results down to the nonrelativistic regime, despite the slightly incorrect transformation (Nava et al. 2013) of the internal energy to the central engine frame. The "dynamical" isotropic equivalent energy $E_{\rm dyn}$ here was defined as $E_{\rm dyn} = (E_0 - E_3)(1-\cos\theta_j(R_0))/(1-\cos\theta_j(R))$, where E_3 is the reverse-shocked material isotropic equivalent total energy (except the rest-mass energy) in the central engine frame (the effects of side expansion were accounted for by the other factors in parentheses); that is, $E_3 = \Gamma_{3,\rm eff} E'_{\rm int,3} + (\Gamma_3 - 1)E_0/\Gamma_0$, where, again, $\Gamma_{3,\rm eff} = (\hat{\gamma}\Gamma_3^2 - \hat{\gamma} + 1)/\Gamma_3$ provides the correct relativistic transformation of the internal energy. This essentially means that we assumed all energy lost by the reverse-shocked material in this phase to be immediately transferred to the forward-shocked region, contributing to its expansion. For region 2, in this phase, we accounted for the changing adiabatic index in the transition from the relativistic to the nonrelativistic regime by adopting a simple fitting function (Pe'er 2012) $\hat{\gamma} = \hat{\gamma}(\Gamma)$ (reported in the cited paper). This gives a more accurate estimate of the sound speed to be used in Equation (C3) in this phase.

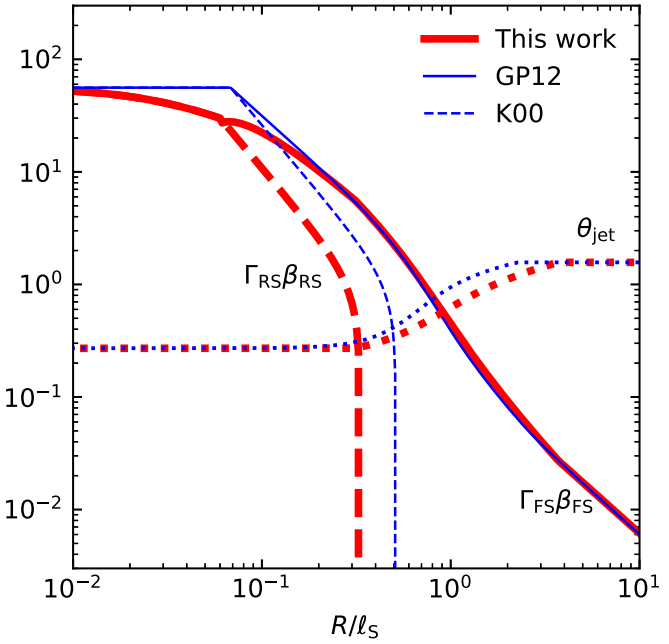

Figure 9. Comparison between our shock dynamics and those from models in the literature. Red lines show the forward shock four-velocity (i.e., $\Gamma\beta$; solid), reverse shock four-velocity (dashed), and jet half-opening angle (dotted) as a function of the shock radius (in units of the Sedov length) as computed with our model for our best-fit parameters $E_0 = 2.5 \times 10^{53}$ erg, $\Gamma_0 = 57$, and $n = 0.21\ {\rm cm}^{-3}$. Blue lines show the same quantities computed following Granot & Piran (2012; their "trumpet" model) for the forward shock Lorentz factor and jet opening angle and Kobayashi (2000) for the reverse shock Lorentz factor.

Figure 9 shows a comparison of the forward shock dynamics computed with our model to that predicted by the "trumpet"

model in Granot & Piran (2012, hereafter GP12) and the reverse shock dynamics compared to the simple analytical estimate from Kobayashi (2000, hereafter K00). The results are similar, though some differences are apparent; the side expansion predicted by our model is somewhat slower, and the initial deceleration is markedly different, since the GP12 model does not account for the reverse shock.

C.4.3. Computation of the Light Curves

The dynamical computations described above give the Lorentz factor of the shock, $\Gamma_s(R)$, and shocked material, $\Gamma(R)$, as functions of the radius R (the distance from the central engine) for each shock (forward and reverse), plus the effective comoving thickness $\Delta'(R)$ of the shocked region, the comoving internal energy density $e'_{\rm int}(R)$, and the electron number density $n'_{\rm e}(R)$ behind the shock. Given these quantities, we computed the comoving specific emissivity $j'_{\nu'}(R)$ behind the shock by assuming (i) a fraction $\chi_{\rm e}$ of electrons to be accelerated into an isotropic, power-law energy distribution with index p, that is, $dn'_{\rm e}/d\gamma \propto \gamma^{-p}$ (where γ is the electron Lorentz factor as measured in the comoving frame) extending from $\gamma_{\rm m}$ to $\gamma_{\rm max}$, and to hold a constant fraction $\epsilon_{\rm e}$ of the postshock energy density at any radius, and (2) an effectively isotropic magnetic field B to be generated by small-scale turbulence, again holding a constant fraction $\epsilon_{\rm B}$ of the postshock energy density. These assumptions led to the definition of the injected electron power-law minimum Lorentz factor,

$$\gamma_{\rm m} = \frac{1-\kappa^{1-p}}{1-\kappa^{2-p}}\frac{p-2}{p-1}\frac{\epsilon_{\rm e}}{\chi_{\rm e}}\frac{e'_{\rm int}}{n'_{\rm e}m_{\rm e}c^2}, \tag{C7}$$

where $m_{\rm e}$ is the electron rest mass, and $\kappa = \gamma_{\rm max}/\gamma_{\rm m}$ is taken as a free parameter. Whenever this value fell below 1, we considered an effective injection Lorentz factor $\gamma_{\rm m,eff} = 1$ and an effective number of synchrotron-emitting electrons (Sironi & Giannios 2013) $\chi_{\rm e} n'_{\rm e,\,eff} = (1-\kappa^{1-p})(p-2)\epsilon_{\rm e}e'_{\rm int}/(1-\kappa^{2-p})(p-1)m_{\rm e}c^2$ (this is relevant early in the reverse shock in the thin shell regime and at late times in the forward shock in the so-called "Deep Newtonian" phase; Sironi & Giannios 2013). The effective electron cooling Lorentz factor $\gamma_{\rm c}$ was computed as

$$\gamma_{\rm c} = \frac{6\pi m_{\rm e}c}{\sigma_{\rm T}B^2t'(1+Y)}, \tag{C8}$$

where $\sigma_{\rm T}$ is the Thomson cross section, t' is the comoving time elapsed since the explosion, and Y is the ratio of the comoving synchrotron radiation energy density. To account for the Klein–Nishina suppression of the cross section for photons with energy above $m_{\rm e}c^2$ in the electron comoving frame, we computed Y including only the radiation energy density of photons below $\nu'_{\rm KN} = m_{\rm e}c^2/h\gamma_{\rm c}$. This turned Equation (C8) into an equation for the quantity $\gamma_{\rm c}(1+Y(\gamma_{\rm c}))$, which we solved numerically to obtain $\gamma_{\rm c}$ self-consistently. The electron energy distribution at a given radius, accounting for the effect of cooling, was thus assumed to have the form

$$\frac{dn'_{\rm e}}{d\gamma} = \frac{\chi_{\rm e}n'_{\rm e}}{\gamma_{\rm p}\xi}\,\Xi(\gamma,\,\gamma_{\rm m},\,\gamma_{\rm c},\,p), \tag{C9}$$

where $\xi = \int_1^\infty \Xi\, d(\gamma/\gamma_{\rm p})$, and

$$\Xi = \begin{cases} (\gamma/\gamma_{\rm p})^{-q} & \gamma_{\rm p} < \gamma < \gamma_0 \\ (\gamma_0/\gamma_{\rm p})^{-q}(\gamma/\gamma_0)^{-p-1} & \gamma_0 < \gamma < \gamma_{\rm max}, \\ 0 & \text{otherwise} \end{cases} \tag{C10}$$

where $\gamma_{\rm p} = \min(\gamma_{\rm m},\,\gamma_{\rm c})$, $\gamma_0 = \max(\gamma_{\rm m},\,\gamma_{\rm c})$, and $q = 2$ if $\gamma_{\rm c} < \gamma_{\rm m}$ or $q = p$ otherwise. The synchrotron emissivity of these electrons was assumed to be given by

$$j'_{\nu',\rm syn} = \frac{\chi_{\rm e}n'_{\rm e}m_{\rm e}c^2\sigma_{\rm T}B}{6e\xi}S_{\nu'}, \tag{C11}$$

where e is the electron charge, $\sigma_{\rm T}$ is the Thomson scattering cross section, and

$$S_{\nu'} = \left[C_1^s\left(\frac{\nu'}{\nu'_{\rm p}}\right)^{-s/3} + C_2^s\left(\frac{\nu'}{\nu'_{\rm p}}\right)^{s(q-1)/2}\right]^{-1/s} \times \left[1+\left(\frac{\nu'}{\nu'_0}\right)^{1-q+p}\right]^{-1/2}\exp\left(-\sqrt{\frac{\nu'}{\nu'_{\rm max}}}\right), \tag{C12}$$

where $\nu'_{\rm p} = \gamma_{\rm p}^2 eB/2\pi m_{\rm e}c$, $\nu'_0 = \gamma_0^2 eB/2\pi m_{\rm e}c$, $s = (q/3)^{-3/2}$, $C_1 = 5(q-1/3)/12$, and $C_2 = (4/3)^q/2$. This is a fitting formula that approximates the exact spectral shape of the synchrotron emission (Rybicki & Lightman 1979) from the electron distribution in Equation (C9), and we include an exponential cutoff at the synchrotron burn-off (de Jager et al. 1996) frequency $\nu'_{\rm max} = 30$ MeV. Compared to the usual broken power-law approximation employed in the literature (Sari et al. 1998; Granot et al. 1999; Panaitescu & Kumar 2000), this gives a more accurate representation of the transitions between different spectral regimes. The synchrotron self-Compton emissivity was assumed to be

$$j'_{\nu',\rm ssc} = \frac{m_{\rm e}c^2}{3e}\frac{\sigma_{\rm T}^2\chi_{\rm e}^2 n_{\rm e}'^2}{4\pi\gamma_{\rm p}}B\frac{\zeta}{\xi^2\lambda}\times \times \int_{\gamma_{\rm KN}}^{\gamma_{\rm max}}\Xi(\gamma/\gamma_{\rm p})S_{\nu'}\left(\frac{3\nu'}{4\gamma^2}\right)d\gamma, \tag{C13}$$

where $\lambda = \int_0^\infty S_{\nu'}d\nu'$, $\zeta = \int_1^{\gamma_{\rm max}/\gamma_{\rm p}}(\gamma/\gamma_{\rm p})^2\,\Xi\, d(\gamma/\gamma_{\rm p})$, and $\gamma_{\rm KN} = 3h\nu'/4m_{\rm e}c^2$ is the electron Lorentz factor below which Compton scattering at frequency ν' is suppressed by the Klein–Nishina effects. The total emissivity is $j'_{\nu'} = j'_{\nu',\rm syn} + j'_{\nu',\rm ssc}$.

For the reverse shock, during the adiabatic expansion phase that follows the shock crossing, we expect no more electrons to be injected into region 3 and no further acceleration to take place. Moreover, since the magnetic field energy density is thought to reach $\epsilon_{\rm B}e'_{\rm int,3}$ by means of amplification by turbulence behind the shock, it is reasonable (Chang et al. 2008) to expect $\epsilon_{\rm B}$ not to remain constant after the shock crossing. For these reasons, we assumed the Lorentz factors $\gamma_{\rm m}$ and $\gamma_{\rm c}$ to evolve as $\gamma_x(R) \propto \gamma_x(R_\oplus)(V'_3(R)/V'_{3,\oplus})^{-1/3}$, where $x = m,\,c$, and the $\oplus$ subscript denotes the quantities at the end of the shock crossing; that is, we assumed the electron energy distribution evolution to be dominated by adiabatic cooling. We also neglected any emission from electrons above $\gamma_{\rm c}$, as no electrons above this energy are injected. Finally, we assumed the magnetic field to decay as $B_3(R) = B_{3,\oplus}(V'_3(R)/V'_{3,\oplus})^{-\eta_{\rm B}/2}$,

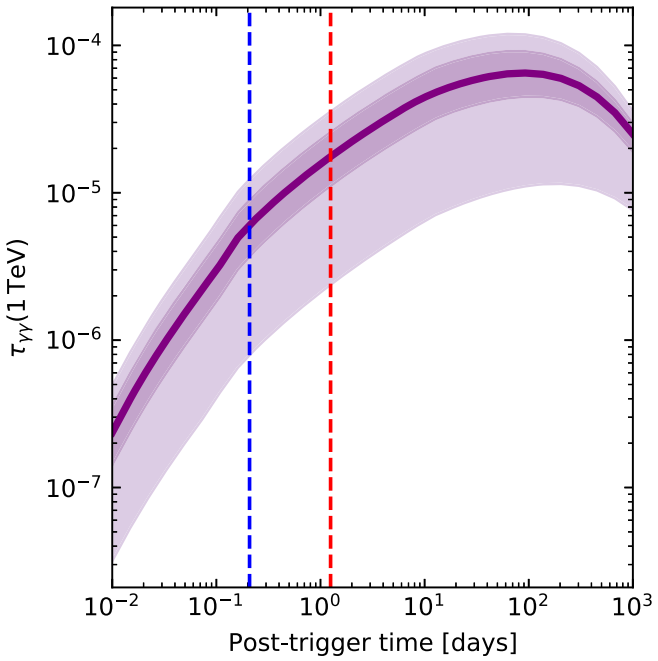

Figure 10. Photon–photon annihilation optical depth for 1 TeV photons. The purple line shows the optical depth to photon–photon annihilation for photons of 1 TeV observed energy produced in the forward shock downstream as a function of the observed time after the gamma-ray trigger. The bands show the 50% (darker band) and 90% (lighter band) uncertainty propagated from the modeling uncertainties. The vertical dashed lines show the times of the HESS observations, namely, 5 (blue) and 30 (red) hr.

where η_B is a constant that parameterizes our ignorance of the magnetic field decay in this phase. The frequency-dependent synchrotron self-absorption optical depth was computed as $\tau_{\nu'} = \alpha_{\nu'}\Delta'$. Here $\alpha_{\nu'}$ is the appropriate absorption coefficient (Rybicki & Lightman 1979), which we decompose into $\alpha_{\nu'} = a_0 a_{\nu'}$, where

$$a_0 = 3^{((p+1)/2)}\left(\frac{1.8}{p^{0.7}} + \frac{p^2}{40}\right)\frac{(p-1)\pi^{3/2}e\,\chi_e n_e'}{\gamma_p^5 B} \tag{C14}$$

and

$$a_{\nu'} = \begin{cases} \left(\dfrac{\nu'}{\nu_p'}\right)^{-5/3} & \nu' < \nu_p' \\ \left(\dfrac{\nu'}{\nu_p'}\right)^{-(q+4)/2} & \nu_p' < \nu' < \nu_0'. \\ \left(\dfrac{\nu_0'}{\nu_p'}\right)^{-(q+4)/2}\left(\dfrac{\nu'}{\nu_0'}\right)^{-(p+5)/2} & \nu_p' < \nu' < \nu_0' \end{cases} \tag{C15}$$

The dependence on p in Equation (C14) is a fitting function (Ghisellini 2013) to the exact expression (Rybicki & Lightman 1979). The comoving surface brightness at the shock was computed as $I_{\nu'}' = ((1-\exp(-\tau_{\nu'}))/\tau_{\nu'})j_{\nu'}'\Delta'(R)$. The surface brightness of the shock for an on-axis observer is then $I_\nu(R) = (1+z)\delta^3 I'_{(1+z)\nu/\delta}(R)$, where $\delta = \Gamma^{-1}(1-\beta\cos\theta)$, with $\beta = \sqrt{1-\Gamma^{-2}}$. Here θ is the polar coordinate of a reference frame centered on the central engine whose z-axis coincides with the jet axis (and the line of sight). In order to compute the light curves, we integrated such surface brightness over equal arrival time surfaces. To do so, we first computed the observer time,

$$t_{\rm obs}(R,\theta) = \frac{1}{c}\int_0^R (\beta_s^{-1} - \cos\theta)dR, \tag{C16}$$

where $\beta_s = \sqrt{1-\Gamma_s^{-2}}$, on a grid over the jet surface. For computational efficiency, since most of the emission comes from regions that are closest to the line of sight (due to relativistic beaming), we used a logarithmically spaced grid in θ, which provides finer spacing closer to the line of sight, and with the smallest grid spacing equal to $10^{-2}\Gamma_0^{-1}$, where Γ_0 is the initial jet Lorentz factor. This ensured that the relativistic beaming cones were always resolved. We then numerically inverted the relation between R and $t_{\rm obs}$ on each point of the grid to obtain $R(t_{\rm obs},\theta)$, that is, the equal arrival time surfaces. The afterglow flux density was finally computed as

$$\frac{dF}{d\nu} = \frac{2\pi}{d_L^2}\int_0^{\theta_j} R^2(t_{\rm obs},\theta)I_\nu(R(t_{\rm obs},\theta))\sin\theta d\theta, \tag{C17}$$

where d_L is the luminosity distance.

In Figure 1, we show the predicted size (FWHM) of the radio image entailed by the model. This was computed using the model described in Ghirlanda et al. (2019), which yields more accurate surface brightness distributions, as it includes the integration over the shock profile.

C.5. Photon–Photon Absorption Optical Depth

High-energy photons produced in the shock downstream could have a nonnegligible probability of pair annihilation with lower-energy photons to form electron–positron pairs before being able to escape the region. Therefore, we estimated the optical depth to this form of absorption for photons in the HESS energy range. The optical depth can be written approximately as (Svensson 1987)

$$\tau_{\gamma\gamma}(\nu') = \eta(\nu_a')\sigma_T\frac{dU_{\rm rad}(\nu_a')}{dh\nu'}\Delta', \tag{C18}$$

where h is Planck's constant, $h\nu_a' = (m_e c^2)^2/h\nu'$ is the typical frequency of target photons that can annihilate with those of frequency ν', $\eta(\nu_a')$ is a dimensionless function (Svensson 1987) that depends on the slope of the photon spectrum at ν_a', $U_{\rm rad}$ is the comoving radiation energy density, and Δ' is the comoving thickness of the shell. For photons in the HESS energy band, ν_a' is in the synchrotron range, so we can safely neglect the synchrotron self-Compton contribution to $U_{\rm rad}$. Also, we conservatively assume Δ' to be equal to the entire shell thickness as computed in the forward shock dynamics model described above, even though high-energy photons are mostly produced in a thinner shell closer to the shock, as fast enough electrons typically cool before being advected to the back of the shell. With these assumptions, we have that the optical depth for photons at the observed frequency ν is

$$\tau_{\gamma\gamma}(\nu) = \eta(\nu_a')\frac{m_e c\sigma_T^2}{9eh}\frac{\chi_e n_e' BR^2(\hat\gamma-1)}{\Gamma(\hat\gamma\Gamma+1)}\frac{\zeta}{\xi\lambda}S_{\nu'}(\nu_a'), \tag{C19}$$

with $\nu_a' = \Gamma(m_e c^2)^2/h^2\nu(1+z)$. Figure 10 shows the resulting optical depth for 1 TeV photons as a function of time, including the modeling uncertainties. The vertical dashed lines

mark the times of the HESS observations. We conclude that photon–photon absorption is unimportant for our parameters.

C.6. Afterglow Model Fitting

In order to estimate the parameters of our afterglow model that provide the best fit to the observations and their uncertainties, we adopted an MCMC approach. We assumed a Gaussian log-likelihood model to which each data point contributes an additive term,

$$\ln \mathcal{L}_{\rm i}(x) = -\frac{1}{2}\frac{(F_{\nu,{\rm m}}(x,\,\nu_{\rm i},\,t_{\rm obs,i}) - F_{\nu,{\rm i}})^2}{\sigma_{\rm i}^2 + \rho_{\rm sys}^2 F_{\nu,{\rm m}}^2} + - \frac{1}{2}\ln\left[2\pi(\sigma_{\rm i}^2 + \rho_{\rm sys}^2 F_{\nu,{\rm m}}^2)\right], \quad \text{(C20)}$$

where $F_{\nu,{\rm i}}$ is the ith flux density measurement, corresponding to frequency $\nu_{\rm i}$ and observer time $t_{\rm obs,i}$, or the flux integrated in the 0.3–10 keV band in the case of XRT data points (for these, we also include the photon index, with a term of the same form but with no assumed systematic contribution to the uncertainty), and $\sigma_{\rm i}$ is the associated 1σ uncertainty (if asymmetric, the appropriate value is used depending on the sign of $F_{\nu,{\rm m}} - F_{\nu,{\rm i}}$). In the case of upper limits, we used a simple one-sided Gaussian penalty of the form

$$\ln \mathcal{L}_{\rm i} = \begin{cases} 0, & F_{\nu,{\rm m}} - F_{\nu,{\rm i}} \leqslant 0 \\ -\frac{1}{2}\frac{(F_{\nu,{\rm m}}(x,\,\nu_{\rm i},\,t_{\rm obs,i}) - F_{\nu,{\rm i}})^2}{0.01^2 F_{\nu,{\rm i}}^2}, & F_{\nu,{\rm m}} - F_{\nu,{\rm i}} > 0 \end{cases}. \quad \text{(C21)}$$

The symbol x here represents all emission model parameters, namely, $x = (E_0,\, n,\, \Gamma_0,\, \theta_{\rm j},\, \epsilon_{\rm e,FS},\, \epsilon_{\rm B,FS},\, p_{\rm FS},\, \chi_{\rm e,FS},\, \epsilon_{\rm e,RS},\, \epsilon_{\rm B,RS},\, p_{\rm RS},\, \chi_{\rm e,RS},\, \eta_{\rm B})$. The additional dimensionless parameter $\rho_{\rm sys}$ represents an unknown systematic contribution to the relative error on all measurements, which is introduced to account for intercalibration uncertainties between different instruments and to avoid data points with very small formal errors to dominate the likelihood. We adopt a log-uniform prior $\pi(\rho_{\rm sys}) \propto \rho_{\rm sys}^{-1}$ between 10^{-10} and 1 and eventually marginalize over this parameter. Due to the very high dimensionality of the problem and the rather expensive computation of the likelihood (which requires the evaluation of the entire dynamics and emission model at a number of times and frequencies), we found keeping all parameters free to be intractable with our computational resources. By manual exploration of the parameter space, we found that $\eta_{\rm B} < 6$ always produced late bumps (Resmi & Zhang 2016) in the radio band, which tended to overproduce the observed flux densities, while for $\eta_{\rm B} \geqslant 6$, these bumps were suppressed, so we fixed $\eta_{\rm B} = 6$. We also found that the standard choice, $\chi_{\rm e,RS} = 1$, did not prevent a good fit of the early X-ray and optical data, so we also kept this parameter fixed. The other 12 parameters were left free to vary, subjected to the priors reported in Table 4. We sampled the resulting posterior probability density using the EMCEE python package (Foreman-Mackey et al. 2013) using 24 walkers, which we ran over 3×10^4 iterations for a total of 7.2×10^5 samples, on a cloud computing facility (Landoni et al. 2018) provided by the Italian National Institute for Astrophysics. The resulting marginalized posterior probability density distributions, after discarding the initial 50% of the chain as burn-in, are shown in orange in the corner plot of Figure 11. After obtaining our solution, we verified that setting $\eta_{\rm B} < 6$ significantly worsened the fit statistics when keeping all other parameters fixed to their best-fit values.

Combining the bulk Lorentz factor estimate from this analysis and the isotropic equivalent energy from Appendix B, we can locate this burst on the $\Gamma - E_{\rm iso}$ plane. Figure 12 compares the result with the sample from Ghirlanda et al. (2018), which shows that this burst is consistent with the extrapolation of the previously observed correlation.

Table 4
Afterglow Parameter Estimation Results

Parameter[a]	Narrow Prior	Wide Prior	Bounds	Prior Type[b]
$E_0/10^{53}$ erg	$2.5^{+1.9}_{-1.3}$	$8.6^{+26.0}_{-6.7}$	$10^{48}-10^{56}$	l. u.
$n/{\rm cm}^{-3}$	$0.21^{+0.37}_{-0.09}$	$0.87^{+4.96}_{-0.63}$	$10^{-6}-10^{2}$	l. u.
Γ_0	$56.6^{+3.3}_{-5.3}$	$55.0^{+3.4}_{-4.7}$	>10	l. u.
$\theta_{\rm j}/{\rm deg}$	$15.4^{+1.2}_{-0.94}$	$15.8^{+1.3}_{-0.9}$	0.6–60	u.
$\epsilon_{\rm e,FS}$	$0.030^{+0.029}_{-0.017}$	$0.008^{+0.003}_{-0.006}$	$10^{-6}-0.6$	l. u.
$\epsilon_{\rm B,FS}/10^{-5}$	$2.5^{+3.5}_{-1.3}$	<0.43	$10^{-6}-0.3$	l. u.
$p_{\rm FS}$	$2.010^{+0.002}_{-0.002}$	$2.010^{+0.003}_{-0.002}$	2.001–2.9	u.
$\chi_{e,{\rm FS}}/10^{-2}$	<6.5	$0.7^{+2.1}_{-0.5}$	$10^{-2}(10^{-10})-10^{0}$	l. u.
$\epsilon_{\rm e,RS}$	$0.28^{+0.32}_{-0.16}$	$0.1^{+0.5}_{-0.08}$	$10^{-6}-0.6$	l. u.
$\epsilon_{\rm B,RS}/10^{-3}$	$1.2^{+1.8}_{-0.8}$	$0.3^{+1.0}_{-0.2}$	$10^{-6}-0.3$	l. u.
$p_{\rm RS}$	$2.13^{+0.04}_{-0.08}$	$2.12^{+0.05}_{-0.07}$	2.001–2.9	u.
$\log(\rho_{\rm sys})$	$-1.8^{+0.1}_{-0.1}$	$-1.8^{+0.1}_{-0.1}$	$10^{-10}-10^{0}$	l. u.
$E_{\rm jet}/10^{51}$ erg	$9.4^{+8.9}_{-4.2}$	32^{+120}_{-25}	…	…
$\eta_\gamma/10^{-3}$	$1.1^{+1.2}_{-0.5}$	$0.34^{+1.1}_{-0.26}$	…	…

Notes. The columns report, from left to right, the parameter name and units, best-fit value (maximum a posteriori) with 1σ errors (or 90% upper/lower limits if the 1σ credible interval rails against a lower/upper bound) for the narrow ($10^{-2} \leqslant \chi_{\rm e,FS} \leqslant 1$) and wide ($10^{-10} \leqslant \chi_{\rm e,FS} \leqslant 1$) priors, the bounds used in the MCMC fitting, and the prior type adopted.[b] The quantities below the horizontal line are derived from the fitting parameters.

[a] Credible ranges are computed as the smallest range that contains 68% of the marginalized posterior probability, or 90% for lower/upper limits.

[b] l. u. = log-uniform; u. = uniform.

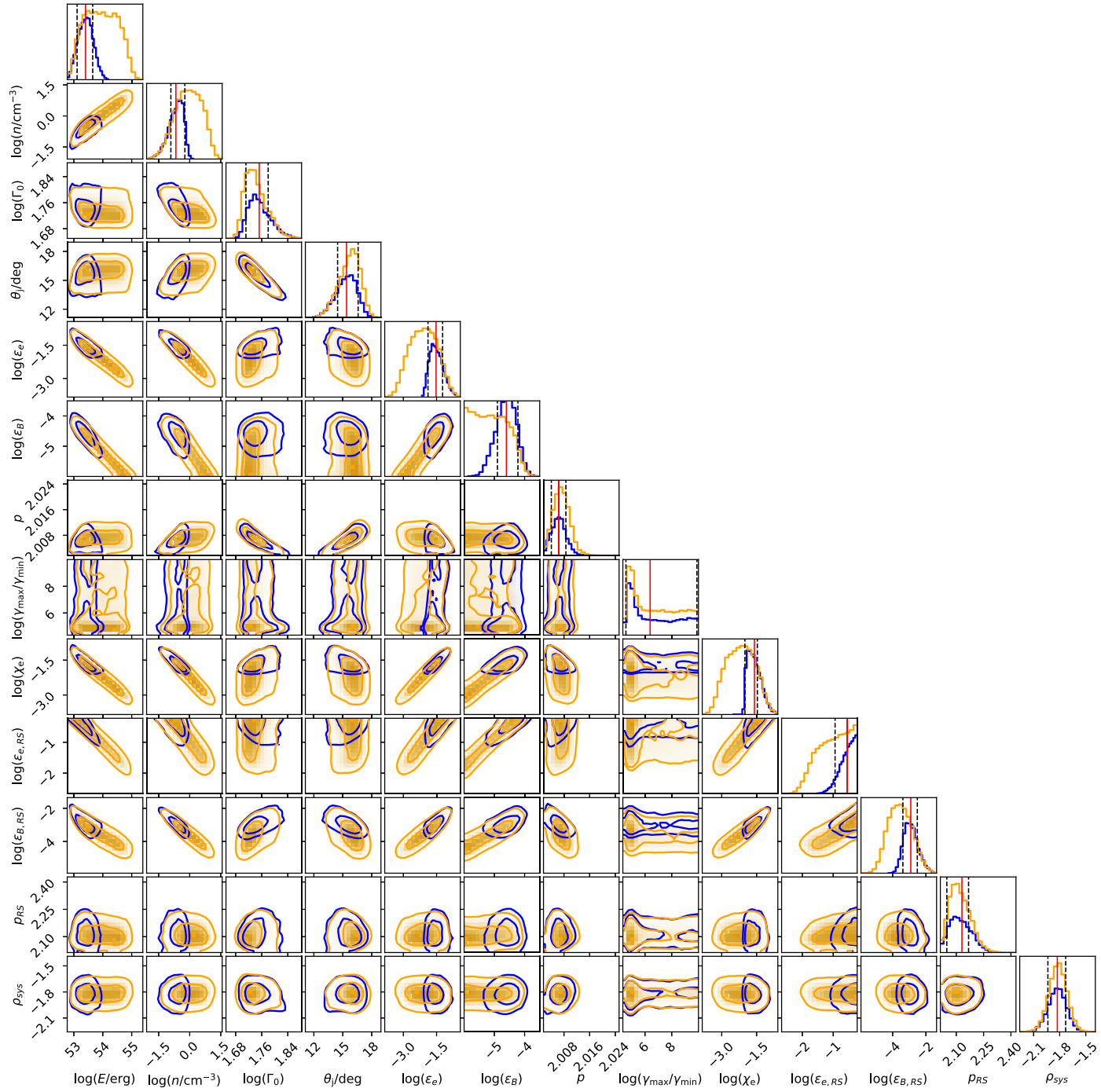

Figure 11. Corner plot of the MCMC posterior sample density distributions. Orange histograms and contours show the results for the wide χ_e prior, while the blue ones are for the narrow prior. The black dashed lines in the plots on the diagonal bracket the 1σ credible interval, while the red solid lines mark the position of the estimated best fit.

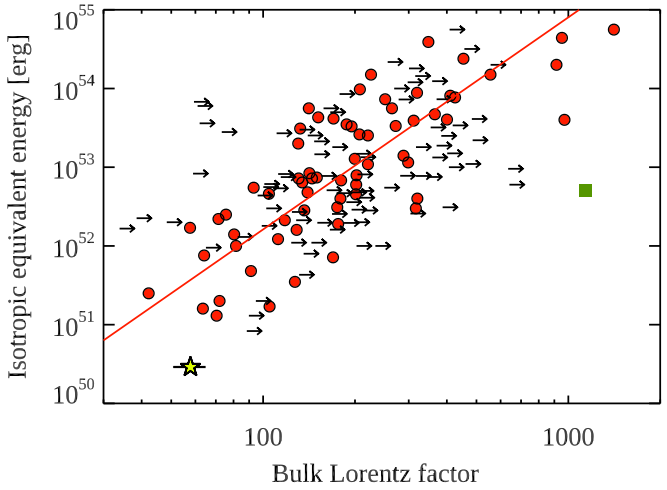

Figure 12. Bulk Lorentz factor. Shown is the correlation between the gamma-ray isotropic equivalent energy and the bulk Lorentz factor for 67 long GRBs (red circles) and one short GRB (green square). The yellow star shows GRB 190829A. Lower limits on Γ_0 are also shown (black arrows). The data are from Ghirlanda et al. (2018). The solid line shows the power law that best fits the red points.

ORCID iDs

Om Sharan Salafia https://orcid.org/0000-0003-4924-7322
Maria Edvige Ravasio https://orcid.org/0000-0003-3193-4714
Jun Yang https://orcid.org/0000-0002-2322-5232
Tao An https://orcid.org/0000-0003-4341-0029
Monica Orienti https://orcid.org/0000-0003-4470-7094
Giancarlo Ghirlanda https://orcid.org/0000-0001-5876-9259
Lara Nava https://orcid.org/0000-0001-5960-0455
Marcello Giroletti https://orcid.org/0000-0002-8657-8852
Prashanth Mohan https://orcid.org/0000-0002-2211-0660
Yingkang Zhang https://orcid.org/0000-0001-8256-8887
Benito Marcote https://orcid.org/0000-0001-9814-2354
Giuseppe Cimò https://orcid.org/0000-0002-1167-7565
Xuefeng Wu https://orcid.org/0000-0002-6299-1263

References

Abdalla, H., Adam, R., Aharonian, F., et al. 2019, Natur, 575, 464
Abdalla, H., Aharonian, F. & HESS collaboration 2021, Sci, 372, 1081
Akaike, H. 1974, ITAC, 19, 716
Alexander, K. D., Laskar, T., Berger, E., et al. 2019, ApJ, 870, 67
An, T., Wu, X.-P., & Hong, X. 2019, NatAs, 3, 1030
Atkins, R., Benbow, W., Berley, D., et al. 2000, ApJL, 533, L119
Barniol Duran, R. 2014, MNRAS, 442, 3147
Beasley, A. J., & Conway, J. E. 1995, in ASP Conf. Ser., 82, Very Long Baseline Interferometry and the VLBA, VLBI Phase-Referencing, ed. J. A. Zensus, P. J. Diamond, & P. J. Napier (San Francisco, CA: ASP), 327
Bell, A. R. 1978, MNRAS, 182, 147
Beniamini, P., Nava, L., & Piran, T. 2016, MNRAS, 461, 51
Blanch, O., Gaug, M., Noda, K., et al. 2020a, GCN, 28659, 1
Blanch, O., Longo, F., Berti, A., et al. 2020b, GCN, 29075, 1
Blanchard, P. K., Berger, E., & Fong, W.-F. 2016, ApJ, 817, 144
Blandford, R. D., & McKee, C. F. 1976, PhFl, 19, 1130
Chand, V., Banerjee, A., Gupta, R., et al. 2020, ApJ, 898, 42
Chang, P., Spitkovsky, A., & Arons, J. 2008, ApJ, 674, 378
Charlot, P., Jacobs, C. S., Gordon, D., et al. 2020, A&A, 644, A159
Chiang, J., & Dermer, C. D. 1999, ApJ, 512, 699
Cunningham, V., Cenko, S. B., Ryan, G., et al. 2020, ApJ, 904, 166
de Jager, O. C., & Harding, A. K. 1992, ApJ, 396, 161
de Jager, O. C., Harding, A. K., Michelson, P. F., et al. 1996, ApJ, 457, 253
de Naurois, M. 2019, GCN, 25566, 1
de Ugarte Postigo, A., Bremer, M., Kann, D. A., et al. 2019, GCN, 25589, 1
Deller, A. T., Tingay, S. J., Bailes, M., & West, C. 2007, PASP, 119, 318
Dichiara, S., Bernardini, M. G., Burrows, D. N., et al. 2019, GCN, 25552, 1
Eldridge, J. J. 2007, MNRAS, 377, L29
Evans, P. A., Willingale, R., Osborne, J. P., et al. 2010, A&A, 519, A102
Fan, Y., & Piran, T. 2006, MNRAS, 369, 197
Fermi GBM Team 2019, GCN, 25551, 1
Fernández, J. J., Kobayashi, S., & Lamb, G. P. 2022, MNRAS, 509, 395
Foreman-Mackey, D., Hogg, D. W., Lang, D., & Goodman, J. 2013, PASP, 125, 306
Fraija, N., Veres, P., Beniamini, P., et al. 2021, ApJ, 918, 12
Frail, D. A., Kulkarni, S. R., Nicastro, L., Feroci, M., & Taylor, G. B. 1997, Natur, 389, 261
Frail, D. A., Kulkarni, S. R., Sari, R., et al. 2000, ApJ, 534, 559
Ghirlanda, G., Nappo, F., Ghisellini, G., et al. 2018, A&A, 609, A112
Ghirlanda, G., Salafia, O. S., Paragi, Z., et al. 2019, Sci, 363, 968
Ghisellini, G. 2013, LNP, 873
Granot, J., & Piran, T. 2012, MNRAS, 421, 570
Granot, J., Piran, T., & Sari, R. 1999, ApJ, 513, 679
Greisen, E. W. 2003, in Astrophysics and Space Science Library, Information Handling in Astronomy - Historical Vistas, AIPS, the VLA, and the VLBA 285, ed. A. Heck (Dordrecht: Kluwer), 109
Heintz, K. E., Fynbo, J. P. U., Jakobsson, P., et al. 2019, GCN, 25563, 1
Hewett, P. C., & Wild, V. 2010, MNRAS, 405, 2302
Hotokezaka, K., Nakar, E., Gottlieb, O., et al. 2019, NatAs, 3, 940
Hu, Y. D., Castro-Tirado, A. J., Kumar, A., et al. 2021, A&A, 646, A50
Huang, Y. F., Dai, Z. G., & Lu, T. 1999, MNRAS, 309, 513
Ignace, R., Cassinelli, J. P., & Bjorkman, J. E. 1996, ApJ, 459, 671
Kalberla, P. M. W., Burton, W. B., Hartmann, D., et al. 2005, A&A, 440, 775
Keimpema, A., Kettenis, M. M., Pogrebenko, S. V., et al. 2015, ExA, 39, 259
Kettenis, M., van Langevelde, H. J., Reynolds, C., & Cotton, B. 2006, in ASP Conf. Ser., 351, Astronomical Data Analysis Software and Systems XV, ed. C. Gabriel et al. (San Francisco, CA: ASP), 497
Kirk, J. G., & Duffy, P. 1999, JPhG, 25, R163
Kirsten, F., Vlemmings, W., Campbell, R. M., Kramer, M., & Chatterjee, S. 2015, A&A, 577, A111
Kobayashi, S. 2000, ApJ, 545, 807
Kobayashi, S., & Sari, R. 2000, ApJ, 542, 819
Kobayashi, S., & Zhang, B. 2003, ApJ, 597, 455
Kovalev, Y. Y., Lobanov, A. P., Pushkarev, A. B., & Zensus, J. A. 2008, A&A, 483, 759
Kumar, P. 1999, ApJL, 523, L113
Lamb, G. P., Mandel, I., & Resmi, L. 2018, MNRAS, 481, 2581
Landoni, M., Genoni, M., Riva, M., Bianco, A., & Corina, A. 2018, Proc. SPIE, 10707, 107070G
Laskar, T., Bhandari, S., Schroeder, G., et al. 2019, GCN, 25676, 1
Lemoine, M. 2013, MNRAS, 428, 845
Lemoine, M. 2015, JPlPh, 81, 455810101
Lesage, S., Poolakkil, S., Fletcher, C., et al. 2019, GCN, 25575, 1
Lu-Lu, Z., Jia, R., Xiao-Li, H., et al. 2021, ApJ, 917, 95
MAGIC Collaboration 2019, Natur, 575, 455
MAGIC Collaboration, Acciari, V. A., Ansoldi, S., et al. 2019, Natur, 575, 455
Martí-Vidal, I., Pérez-Torres, M. A., & Lobanov, A. P. 2012, A&A, 541, A135
Matsumoto, T., Nakar, E., & Piran, T. 2019, MNRAS, 486, 1563
Meegan, C., Lichti, G., Bhat, P. N., et al. 2009, ApJ, 702, 791
Mesler, R. A., & Pihlström, Y. M. 2013, ApJ, 774, 77
Mooley, K. P., Deller, A. T., Gottlieb, O., et al. 2018, Natur, 561, 355
Nava, L. 2018, IJMPD, 27, 1842003
Nava, L., Sironi, L., Ghisellini, G., Celotti, A., & Ghirlanda, G. 2013, MNRAS, 433, 2107
Paek, G. S. H., Im, M., et al. 2019, GCN, 25584, 1
Panaitescu, A., & Kumar, P. 2000, ApJ, 543, 66
Panaitescu, A., & Mészáros, P. 1998, ApJ, 501, 772
Paragi, Z., van der Horst, A. J., Belloni, T., et al. 2013, MNRAS, 432, 1319
Pe'er, A. 2012, ApJL, 752, L8
Petrov, L. 2021, AJ, 161, 14
Planck Collaboration 2016, A&A, 594, A13
Rees, M. J., & Meszaros, P. 1994, ApJL, 430, L93
Resmi, L., & Zhang, B. 2016, ApJ, 825, 48
Rhodes, L., van der Horst, A. J., Fender, R., et al. 2020, MNRAS, 496, 3326
Rybicki, G. B., & Lightman, A. P. 1979, Radiative Processes in Astrophysics (New York: Wiley)
Salafia, O. S., Ravasio, M. E., Yang, J., et al. 2022, Supplementary material: Multi-wavelength view of the close-by GRB 190829A sheds light on gamma-ray burst physics, v1.0, Zenodo, doi:10.5281/zenodo.6412088
Sander, A. A. C., Vink, J. S., & Hamann, W. R. 2020, MNRAS, 491, 4406
Sari, R., & Esin, A. A. 2001, ApJ, 548, 787
Sari, R., Piran, T., & Narayan, R. 1998, ApJL, 497, L17

Sato, Y., Obayashi, K., Yamazaki, R., Murase, K., & Ohira, Y. 2021, MNRAS, 504, 5647
Schlafly, E. F., Meisner, A. M., Stutz, A. M., et al. 2016, ApJ, 821, 78
Shepherd, M. C., Pearson, T. J., & Taylor, G. B. 1994, BAAS, 26, 987
Sironi, L., & Giannios, D. 2013, ApJ, 778, 107
Sironi, L., & Spitkovsky, A. 2011, ApJ, 726, 75
Skrutskie, M. F., Cutri, R. M., Stiening, R., et al. 2006, AJ, 131, 1163
Spitkovsky, A. 2008, ApJL, 682, L5
Svensson, R. 1987, MNRAS, 227, 403
Szomoru, A. 2008, in The 9th European VLBI Network Symposium on The role of VLBI in the Golden Age for Radio Astronomy and EVN Users Meeting (IX EVN Symposium), EXPReS and the e-EVN 072 (Trieste: Sissa), 40
Taylor, G. B., Beasley, A. J., Frail, D. A., Kulkarni, S. R., & Reynolds, J. E. 1999, A&AS, 138, 445
Taylor, G. B., Frail, D. A., Berger, E., & Kulkarni, S. R. 2004, ApJL, 609, L1
Taylor, G. B., Frail, D. A., Kulkarni, S. R., et al. 1998, ApJL, 502, L115
Tsvetkova, A., Golenetskii, S., Aptekar, R., et al. 2019, GCN, 25660, 1
Valeev, A. F., Castro-Tirado, A. J., Hu, Y. D., et al. 2019, GCN, 25565, 1
van Marle, A. J., Langer, N., Achterberg, A., & García-Segura, G. 2006, A&A, 460, 105
Veres, P., Bhat, P. N., Briggs, M. S., et al. 2019, Natur, 575, 459
Wang, X.-G., Zhang, B., Liang, E.-W., et al. 2015, ApJS, 219, 9
Wilms, J., Allen, A., & McCray, R. 2000, ApJ, 542, 914
Wygoda, N., Guetta, D., Mandich, M. A., & Waxman, E. 2016, ApJ, 824, 127
Zhang, B., & Mészáros, P. 2001, ApJ, 559, 110
Zhang, B., Liang, E., Page, K. L., et al. 2007, ApJ, 655, 989
Zhang, B. T., Murase, K., Veres, P., & Mészáros, P. 2021, ApJ, 920, 55